A Real-time Method for Making Engine Exhaust Ash Measurements

A THESIS
SUBMITTED TO THE FACULTY OF THE GRADUATE SCHOOL
OF THE UNIVERSITY OF MINNESOTA
BY

David Daniel Gladis

IN PARTIAL FULFILLMENT OF THE REQUIREMENTS
FOR THE DEGREE OF
MASTER OF SCIENCE

David B. Kittelson

September 2010

Acknowledgements

This project was made possible through gifts by BP-Castrol and Corning and the continued advice and support from Hugh Preston and Timothy Johnson. I would like to thank Dr. Kittelson for the opportunity to work on this project and his continued support and oversight of the project, Dr. Watts for his support and motivation, and James Apple for his hard work during that first summer. I am also grateful to Adam, Luke, Jake, Anil, Darrick, Matthew, and everyone else on the fourth floor for all their advice and support throughout this project and my time in the lab.

Parts of this work were carried out in the College of Science and Engineering Characterization Facility, University of Minnesota, which receives partial support from NSF through the MRSEC program.

Dedication

This thesis is dedicated to my parents for supporting me throughout all my endeavors and Rachel for her continued support.

Abstract

Diesel ash emissions are the non-combustible portion of diesel particulate matter and are mainly derived from metallic lube oil additives such as Ca, Mg, and Zn as well as engine wear metals including Fe. Diesel particulate filters (DPF) are used to filter engine particle emissions and are routinely regenerated, oxidizing the material in the filter. After filter regeneration, metallic ash remains. Over time, this ash can build up in the filter, increasing the filter pressure drop and eventually plugging the filter. Ash emissions can also be used to calculate engine lube oil consumption.

A high temperature oxidation method (HTOM) has been developed to measure ash emissions in real-time. The HTOM uses a tube oven to oxidize the combustible fraction of an engine exhaust sample. The remaining particles are then measured with real-time and near real-time particle sampling techniques.

The HTOM system improvements are discussed along with validation testing and further recommendations regarding improvements in the apparatus and procedure.

Atomized lube oil was used as a test aerosol. Special lube oil blends were formulated to determine measurement sensitivity to specific ash constituents. Ca and Mg were readily detectable by the HTOM. However, the HTOM was not very sensitive to Zn based additives. Chemical equilibrium models show that Ca and Mg formed stable oxides at oven temperatures while Zn went to a gaseous phase.

Repeatability in lube oil spray ash measurements was better than 10 %. Engine exhaust repeats did not show as good repeatability. However engine exhaust is a much less stable and repeatable aerosol.

Steady-state engine ash emissions were sampled from two different Diesel engines (1.9 L VW and Cummins APU) at different speeds and loads. Lube oil doped fuel was also used in the engine tests to artificially increase oil consumption and ash emissions. The engine lube oil consumption was predicted from known lube oil ash concentrations and measured ash emissions. The non-doped fuel tests yielded lower than expected lube oil consumption estimates while the doped tests showed an ash recovery of 31 %.

Transient ash measurements were demonstrated. Ash and soot measurements were made downstream a loading DPF. The downstream soot particle surface area

concentrations tracked better with the ash than soot volume concentrations. Transient engine speed and loads were also measured by the HTOM. Ash diameter concentrations were measured in real-time showing definite spikes of ash emissions at transient load steps.

Table of Contents

List of Tables

List of Figures

Chapter 1: Introduction

1.1 Diesel Exhaust Aerosol

Diesel engine exhaust aerosol is very complex; containing carbonaceous agglomerates, ash, and volatile organic and sulfur compounds (Kittelson, 1998). Figure 1 depicts the evolution of diesel exhaust aerosol on the roadway from combustion to atomspheric dilution and cooling. Carbon particles form during the combustion process but are mostly oxidized. Lubricating oil from the combustion chamber surfaces is evaporated and partially combusted. Metallic species from lube oil, fuel, or engine wear that have been turned to a gas phase during combustion can form particles after cooling. These metallic particles tend to collect on the surface of carbon soot partcles. However, if high enough ash to carbon ratios exist, solid metal nanoparticles can form. During late cooling and atmospheric exhaust dilution small sulfate and volatile organic compounds can nucleate forming nanoparticles.

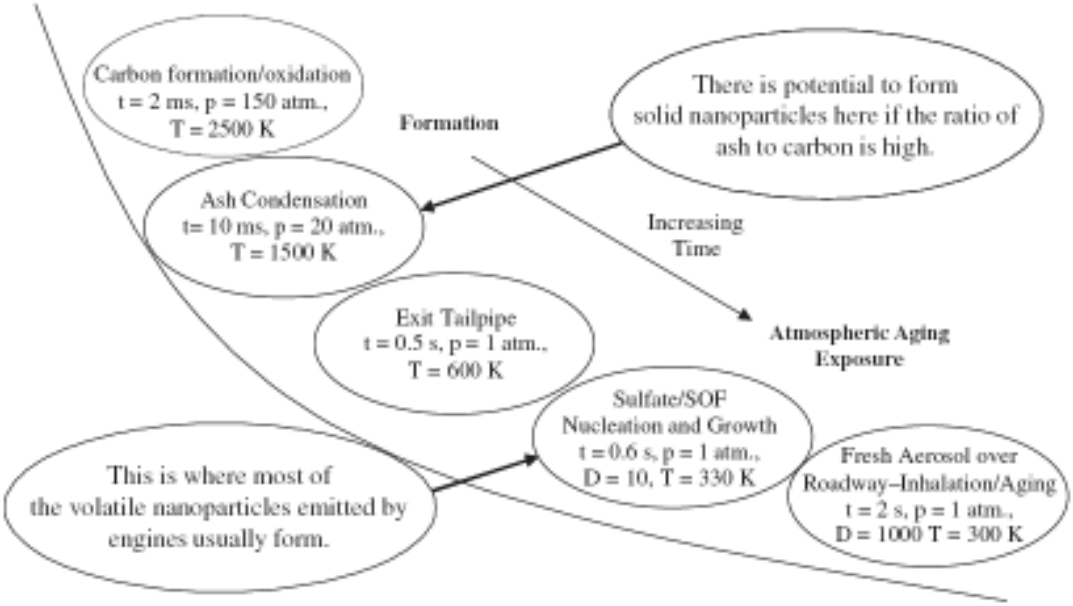

Figure 1: Diesel exhaust particle formation history (Kittelson et al., 2006)

Figure 2 shows a typical Diesel exhaust trimodal particle size distribution weighted for number and mass. The accumulation mode particles account for a majority of the mass concentration and are composed of carbonaceous agglomerates. The

nucleation mode accounts for almost all of the number concentration and is mostly composed of volatile organic species and sulfates that nucleate during exhaust dilution. The coarse mode is composed of material from engine surfaces that are entrained into the exhaust. Figure 3 shows an image of a carbonaceous aglomerate taken by a tranmission electron microscope (TEM). The chain-like agglomerate is composed of spherical primary particles. This sample is from the exhaust pipe of a 1.8 L VW TDI engine opperating on ULSD fuel without an aftertreatment device.

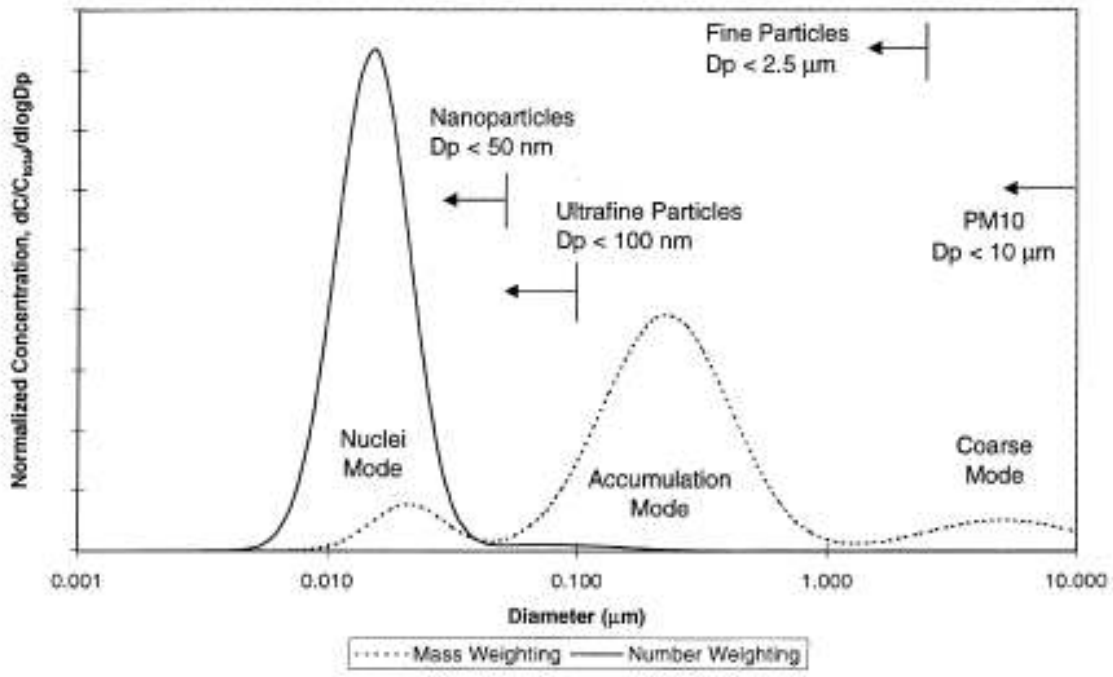

Figure 2: Typical Diesel engine exhaust distribution weighted by both mass and number (Kittelson, 1998)

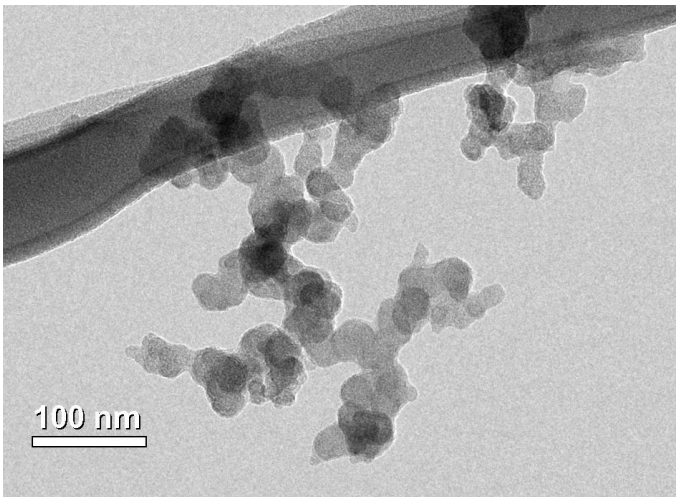

Figure 3: TEM image of a carbon soot agglomerate sampled from Diesel engine exhaust

1.2 Diesel Ash Emissions

Ash can make up between 0.5 and 1.0% of Diesel exhaust particulate matter (Sappok and Wong, 2007). Studies have shown that metallic ash is finely distributed on the surfaces of soot particles (Sappok and Wong, 2007; Miller et al., 2007). Lee et al., (2006) postulated that during combustion metallic species such as engine wear metals and lube oil additives are vaporized. The metals then adsorb or condense on the surface of the carbonaceous agglomerates.

A major source of exhaust ash is metallic lube oil additives (Wang et al., 2003). Other sources include fuel additives and to a lesser extent engine wear metals, sulfates, and phosphates (Bodek and Wong, 2007). Metallic oil additives and engine wear metals can enter the combustion chamber and exhaust through several pathways, some of which are shown in Figure 4. The majority of lube oil is consumed in the power cylinders and valve systems (Hill and Systasma, 1991). Lube oil can enter the combustion chamber through reverse blow-by of the piston rings (De Petris et al., 1996) and is scraped up by the piston rings into the combustion chamber (Wahiduzzaman et al., 1992). Inside the combustion chamber oil evaporates off the cylinder walls and exits with the exhaust as either oil combustion by-products or a non-combusted vapor. Other sources for lube oil consumption include leaks in the valve seals (Hill and Systasma, 1991), turbo charger

bearings, crank case ventilation, and exhaust gas recirculation (EGR) (Krause et al., 1995).

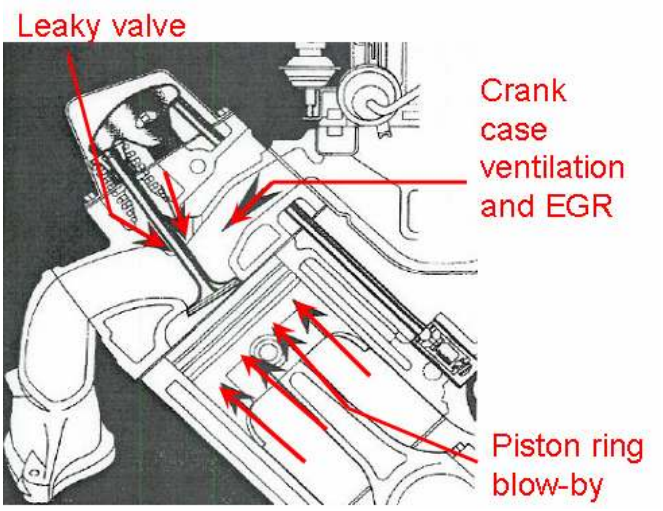

Figure 4: Diagram of lube oil pathways on a typical engine (modified from Hill and Systasma, 1991)

Lube oil additives that contribute to ash emissions are composed of metallic species, P, S, and other elements. Additives are used to improve the performance of the lube oil and include pour point depressants, viscosity modifiers, anti-oxidants, detergents and detergent-inhibitors, dispersants, anti-wear agents, friction modifiers, emulsifiers, demulsifiers, and anti-foam agents (Caines and Haycock, 1996; Pirro and Wessol, 2001). Common metal species that appear in these additives are Ca, Zn, Mg, and Na. Zn is commonly found in the form of a zinc dithiophosphate (ZDDP) which can act as an anti-oxidant and an anti-wear agent that forms an anti-wear coating on engine surfaces at low engine operating temperatures (Varlot et al., 1999). Calcium can be present in sulfonates and phenates acting as detergents (Caines and Haycock, 1996). Magnesium is also commonly used as a detergent (Caines and Haycock, 1996).

Engine ash emissions can foul exhaust aftertreatment devices, and lubricant manufacturers attempt to formulate lube oil to minimize oil consumption and ash production. Exhaust aftertreatment devices are used to meet current emission regulations. One such device is the diesel particulate filter (DPF). The DPF is considered a well developed technology and is currently in the state of cost reduction and

optimization (Johnson, 2009). These filters are typically wall flow monoliths and can be made from cordierite, silicon carbide, and aluminum titanate. Figure 5 shows the flow path through a DPF, with alternating channel plugs forcing flow through the channel walls. To prevent plugging, filters undergo a regeneration process where the PM is oxidized. The noncombustible ash species remain and buildup in the filter. Ash buildup increases exhaust back pressure, which raises fuel consumption rates and reduces engine performance. Ash loading also reduces DPF service life and requires costly mechanical cleaning.

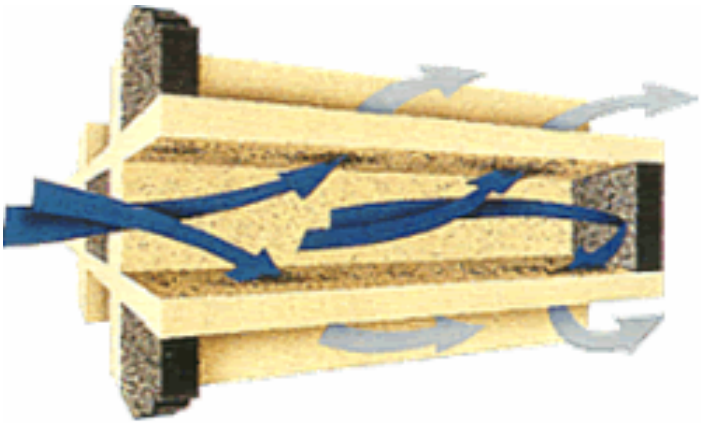

Figure 5: Schematic of flow through a DPF (www.cdc.gov)

Due to the concern of exhaust aftertreatment device poisoning, standards were developed for fuel composition, along with new lube oil formulations to reduce ash formation. On-road Diesel fuel regulations require the use of ultra-low sulfur Diesel (ULSD) fuel with sulfur levels less than 15 ppm. ULSD minimizes sulfate aerosol formation and catalyst poisoning. API CJ-4 is the recommended lubricating oil for use with aftertreatment devices designed to meet the 2007 emission standards. The maximum limits for the API CJ-4 are 1.0% sulfated ash, 0.12% phosphorus, and 0.4% sulfur. Sulfated ash content is defined by ASTM D874 test method which describes a process that includes heating the oil and treating it with sulfuric acid. Both sulfur and phosphorus have been shown to have detrimental effects on exhaust catalysts (Bodek and Wong, 2007).

Several methods are used to measure engine lube oil consumption. Selected methods and literature references are shown in Table 1. The simplest technique is the drain-weigh method where the mass of the lube oil in an engine is measured before and after operation by completely draining the oil sump (Köch, 1993; Weng and Richardson, 2000). However, this method requires very long run-times for accuracy. Other methods use specific tracers in the lube oil that can be measured in the exhaust. A mass balance can then be completed relating the exhaust measurement to lube oil consumption. Radioactive tritium has been used as a tracer but is accompanied by the complications involved with handling radioactive material (Shore, 1988). Sulfur can be used as a tracer in conjunction with low or zero sulfur fuel (Ariga et al., 1992; Froelund et al., 2001). Other tracer methods include the use of metallic lube oil additives such as Ca, Zn, P, and Mg (Andrews et al., 1998; Givens et al., 2003; Okada et al., 2003; Stetter et al., 2003). Manni et al. (2006) reported that measuring lube oil consumption and then calculating DPF ash loading based on oil composition over predicted DPF ash mass gain. Using sulfur or metallic additives requires detailed lube oil analysis to relate to lube oil consumption. The other caveat is that lube oil consumption is not necessarily constant throughout use and composition. It has been shown that the more volatile fraction of the base stock are consumed at a higher rate initially and certain metallic additives such as Zn can be consumed at a higher rate initially and a lower rate in the long term compared to other additives (Givens et al., 2003).

Table 1: Summary of published oil consumption measurements

Shore, 1988 Radioactive tracer technique
Ariga et al., 1992 Sulfur tracer technique
Köch, 1993 Review of drain-weigh, constant-level-sucking/top-up/overflow methods, and radioactive/sulfur tracer methods Implemented constant-level method with capacitance oil level sensor
Andrews et al., 1998 Calcium mass balance between lube oil content and exhaust sampled on a paper filter (tracer)
Weng and Richardson, 2000 Review of gravity fed, oil level change rate, oil pump, drain-weigh, and dipstick level methods Impelemented "Cummins smart oil consumption measuring system" constant oil sump volume, measuring oil flow into reservior
Froelund et al., 2001 Sulfur tracer technique
Gilles et al., 2007 Radionuclide technique in real-time

Numerous studies have examined the mechanisms for ash deposition in DPFs. The axial ash distribution along a DPF is a function of several factors including the method of regeneration. Active or thermal regeneration introduces extra fuel into the exhaust or uses other methods to promote the oxidation of PM by raising exhaust temperatures while passive or catalytic regeneration uses a catalyst. Studies have shown that ash accumulates near the outlet of filters in active systems and more uniformly in passive systems (Bartley et al., 2004). It has also been reported that ash deposition characteristics are affected by filter temperatures and pressure drops (Sappok et al., 2009). Ishizawa et al. (2009) proposed and tested a hypothesis for the differences of ash loading trends between active and passive systems and found that a DPF with a high porosity substrate and an active regeneration system will result in permeable ash loaded to the rear of the DPF; effectively reducing the rate of pressure drop increase due to ash loading. Gaiser and Mucha (2004) reported the development of a DPF pressure drop

model that includes ash deposition. Bartley et al., (2004) reported differences in ash loading between two different types of catalyzed aftertreatment devices. They also reported that Mg based oil detergents produced more ash and greater filter pressure drop increases than Ca based detergents. No explanation was hypothesized. Heibel and Bhargava (2003) described the geometric design of a DPF to minimize effects from ash loading. Kimura et al., (2006) studied ash accumulation of DPFs in real-world conditions concluding that for well maintained vehicles with relatively low oil consumption, vehicle use is the best correlation for ash loading.

The chemical composition of ash deposits in used DPFs has also been studied. Table 2 summarizes studies that have identified exhaust ash composition. Lambert et al., (2010) found $CaSO_4$, $Ca_{19}Zn_2(PO_4)_{14}$, and $CaZn_2(PO_4)_2$ as major ash species in a loaded filter. Manni et al., (2006) reported the presence of zinc phosphates and calcium sulfates in large amounts and magnesium presence as a phosphate. Based on ash composition, it becomes clear that lube oil additive chemistries play an important part in ash composition (Sappok et al., 2009).

Table 2: Reported exhaust ash compositions

Study:	Ash Composition:
Sappok et al., 2009	$CaSO_4$, ZnO, $MgZn_2(PO_4)_2$, $MgSO_4 \cdot 6H_2O$
Lambert et al., 2004	Fe, Cu, Ca, Zn, and Mg
Lambert et al., 2009	$CaSO_4$, $Ca_{19}Zn_2(PO_4)_{14}$, and $CaZn_2(PO_4)_2$
Manni et al., 2006	Zn phosphates and Ca sulfates (hydrated and non-hydrated form), Mg in sulfate form
McGeehan et al., 2009	Ca, Mg, P, S, Zn, and Mo; Ca Sulfate, Zn and Mg Phosphate, and Zn Pyrophosphate; Traces of wear metals
Givens et al., 2003	$CaSO_4$, $Ca_xCu_y(PO_4)_z$,$Ca_xFe_yO_z$, Fe_2O_3, Fe_3O_4. $Zn_2Mg(PO_4)_2$, $Ca_xCu_y(PO_4)_z$
Ishizawa et al., 2009	AlO_3, CaO, Al_2O_3, ZnO

Because most exhaust ash is derived from lube oil additives, there is an important relationship between engine lube oil consumption and ash emissions. The measurement of ash emissions can be used to estimate lube oil consumption as well as to predict DPF ash loading. Rates for diesel engine lube oil consumption have been reported as 0.3-1.5 g/hr during steady-state engine testing and 7-40 g/hr for high speed Diesels (Stetter et al., 2003) and over 1000 g/hr (0.2 to 0.7 g/kW-hr) during high load testing of locomotive Diesel engines (Froelund et al., 2003). From data presented in Givens et al., 2003, lube oil consumption in a passenger sized diesel engine during a mixed driving cycle was approximately 7 g/hr based on an average speed and oil density assumption.

Numerous qualitative and quantitative methods are used to measure engine ash emissions. Okada et al., (2003) used Inductively Coupled Plasma Mass Spectrometry (ICPMS) to analyze PM captured on a filter for trace metal composition. This method requires a sample to be taken on a filter and analyzed later, introducing a large time delay, poor resolution, and possible errors with sample handling. An Aerosol Time-of-Flight Mass Spectrometer (ATOFMS) has also been used to carry out real-time particle size and composition measurements (Okada et al., 2003). The ATOFMS is very expensive and can only analyze one particle at a time requiring fairly long steady state samples to attain a true size and composition distribution. Lombaert et al., (2004) compared Time Resolved Laser Induced Break-down Spectroscopy (TRELIBS) with Scanning Electron Microscopy with Energy Dispersing spectrometry (SEM/EDS) for analyzing the metal species of Diesel engine exhaust that were collected on a filter. Miller et al., (2007) used a combination of Transmission Electron Microscopy (TEM) and Energy Dispersive Spectroscopy (EDS) to examine morphology and elemental composition of specific engine exhaust particles containing metal. Lambert et al., (2010) completed post mortem analysis of ash deposited in a DPF including x-ray scans of a used filter, filter surface area analysis, x-ray fluorescence (XRF), and X-ray Diffraction (XRD); Electron Probe Micro Analysis (EPMA) and Field Emission Gun Scanning Electron Microscopy (FEG-SEM) were also used.

We have developed a high temperature oxidation method (HTOM) to make engine exhaust ash measurements (Kim, 2005; Filice et al., 2007; Apple et al., 2009;

Gladis and Kittelson, 2009). This method has the capability to track engine ash emissions and approximate lube oil consumption in real-time over transient engine conditions. A similar methodology has been used to study soot oxidation kinetics (Jung et al., 2003). Kim, (2005) used the HTOM to determine the initial feasibility of measuring engine ash emissions by first testing the survival of $CaCl_2$ particles through a tube furnace at temperatures up to 1200ºC and then sampling exhaust from an engine with lube oil doped fuel. A mass balance analysis for the engine tests determined a 47% ash survival rate for the system used in Kim (2005). Filice et al., (2007) performed more fundamental calibration experiments by using the HTOM to sample different laboratory generated metallic aerosols. The survival of $MgCl_2$ and $MgSO_4$ particles were examined for tube oven temperatures from 25 to 1100ºC. Particle volume concentration reductions of 94% and 89% were reported for $MgCl_2$ and $MgSO_4$ respectively.

The HTOM method for measuring ash has advantages over other methods. It enables metallic ash to be measured in real or near real-time without chemical tracers, special fuel or oil blends, or engine modifications. It enables ash measurement during transient exhaust events. It is cost effective compared to other methods and does not require the post analysis of samples taken during a test.

1.3 HTOM overview

The HTOM uses a high temperature tube furnace to oxidize the combustible fraction of a continuous aerosol. With a sufficient residence time at high enough temperatures, near complete oxidation of the non-metallic fraction is achieved, leaving only metallic ash particles. Near real-time and real-time particle measurement techniques can be used to quantify the remaining ash particles. Figure 6 shows a basic diagram of the HTOM. Particle measurements can be taken upstream and downstream of the oven to determine the metallic ash fraction of the aerosol.

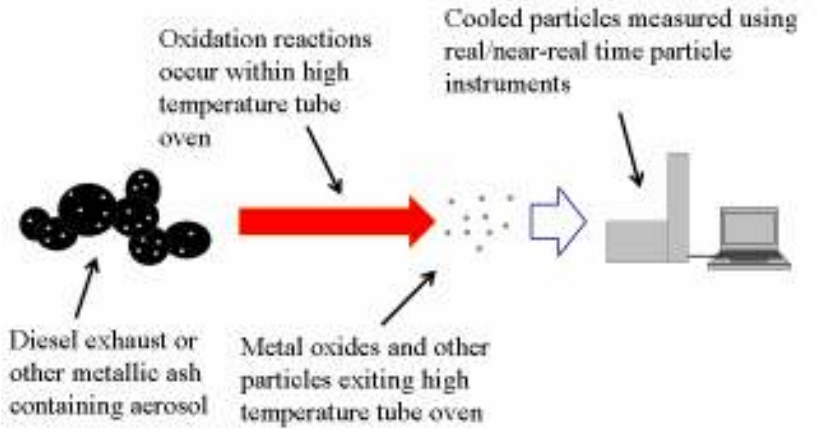

Figure 6: General diagram of the HTOM

1.4 Objectives

Research covered in this thesis improves, validates, and demonstrates the utility of the HTOM. The following developmental challenges are addressed:

- Minimization of particle loss
- Improvement of oxidation kinetics
- Improvement of the signal-to-noise ratio
- Improvement of measurement repeatability

System and method improvements will be discussed accompanied by experimental validation. Atomized lube oil and engine exhaust were used for characterization and validation of the HTOM. Experiments to be discussed include:

- Repeatability and sensitivity characterization using atomized lube oil containing known quantities of specific additives
- Comparison of ash content from fresh and used commercially available lube oils
- Repeatability characterization sampling steady-state engine exhaust
- Real-time ash measurements from steady-state engine exhaust
- Real-time transient engine ash measurements
- Ash penetration measurements from a loading DPF

The apparatus, procedure, and methodology for each experiment will be covered

along with general methods. Results are given along with a discussion.

Chapter 2: Apparatus, procedure, and methods

2.1 Project overview

Due to the diverse interests of the sponsors funding the HTOM developmental project, two separate directions were taken. To gain a more fundamental understanding of the HTOM the kinetics of metallic elements in the tube oven was studied by analyzing the survival of specific metallic compounds in the oven and completing basic chemical equilibrium models for the metallic species. The HTOM was also applied to measure real world engine exhaust aerosols. Experiments were conducted to evaluate ash emissions from a steady-state engine, transient engine, and a loading DPF. The fundamental and application based studies were performed in parallel. Both types of research led to method and apparatus improvements. Figure 7 shows a timeline that gives the chronological order in which experiments were performed alongside experimental improvements and other major events. This is especially of interest in the following section that describes changes and improvements to the apparatus and methods. Major apparatus events include condensation particle counter instrument (CPC) change, tube oven replacement, tube oven temperature profile improvement, and the rebuilding of the VW fuel pump after a leak was detected.

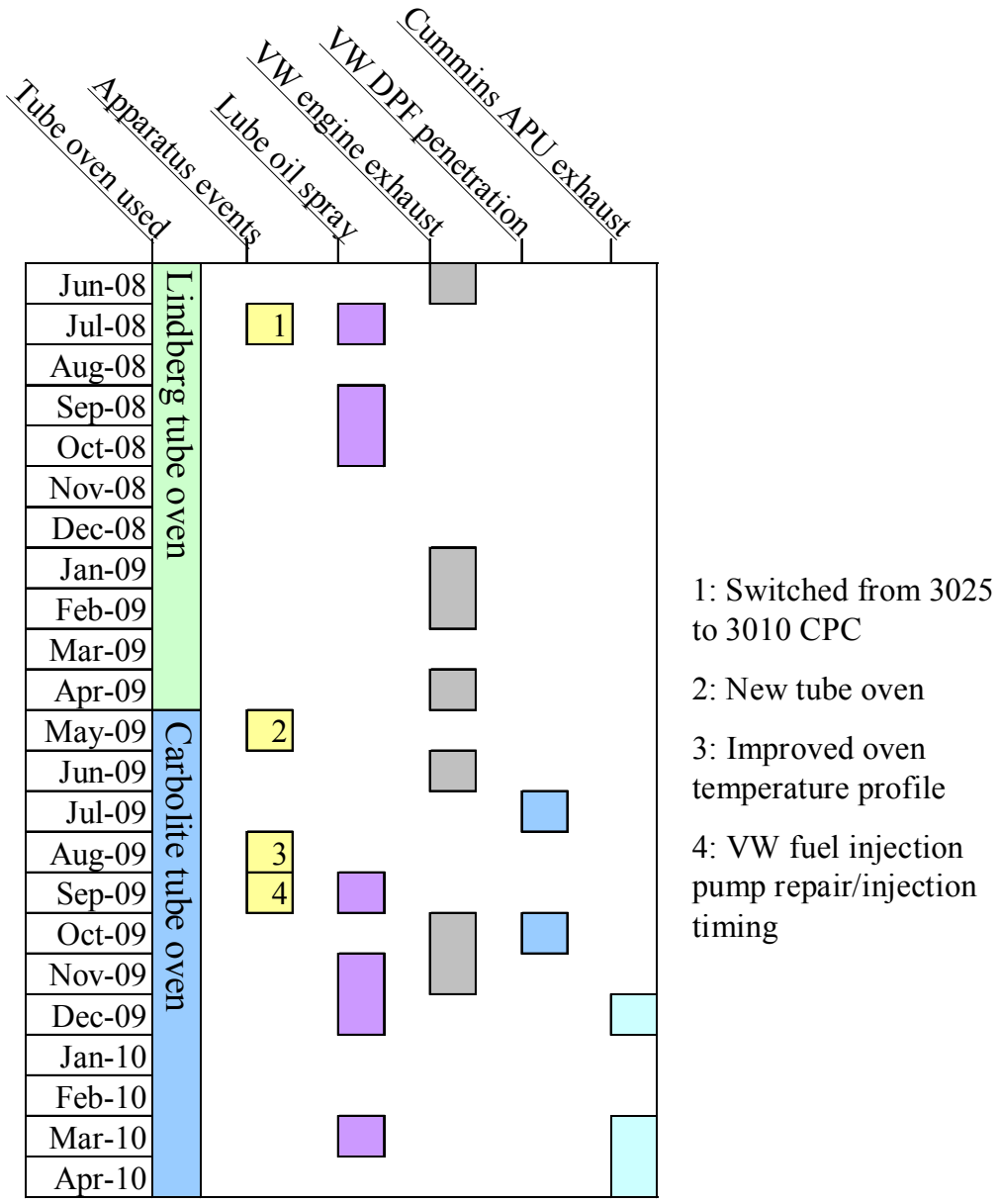

Figure 7: Timeline for HTOM experiments in reference to major apparatus improvements and events

2.2 System improvements: apparatus and methods

The high temperature oxidation method (HTOM) apparatus includes a quartz tube inside of a tube oven. Initially, a Lindberg/Blue M Model HTF55122A oven with a Model CC58114A-1 control module was used. The original tube had an internal diameter of 10.3 mm and the original flow rate was 2 L/min. The temperature profile of

the gas inside the tube is shown in Figure 8. Based on this temperature profile and flow rate the particle residence time inside the heated length was calculated to be 0.2 s for the 1100 °C condition. The heated length was arbitrarily defined as the distance in which the temperature was equal to or greater than 90 % of the set temperature of 1100 °C.

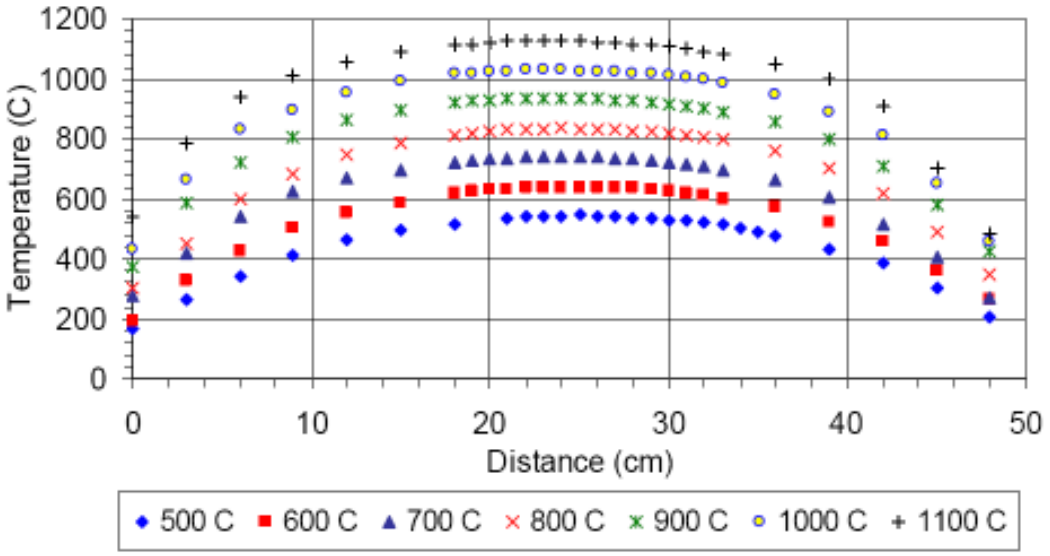

Figure 8: Temperature profile of air inside 10.3 mm ID quartz work tube at 2 L/min using Lindberg tube oven as measured by (Kim 2005)

The Lindberg oven was replaced by a new Carbolite CTF 12-65-550 tube oven. The Carbolite oven offered the same maximum temperature (1200 ºC) as the Lindberg furnace, but featured a greater heated length (550 mm) and a larger diameter (65 mm) to allow clearance for tubes with greater diameters. Both of these features allowed for longer particle residence times inside of the heated portion of the oven. Initially, a quartz work tube with an ID of 16.7 mm was used in the Carbolite oven. It was determined that modifications were needed with this set-up to reduce heat losses at the inlet and outlet of the tube oven. High temperature insulation was packed in the ends of the furnace between the work tube and the inner diameter of the tube oven.

The temperature profiles measured inside the Carbolite tube oven are shown in Figure 9 for an oven set-point temperature of 1100 ºC. The temperature profiles were measured with a 1 L/min sample flow by thermocouples placed inside and outside of the work tube. The major benefit of using additional insulation is to flatten the temperature

profile and increase the residence time of the aerosol at or near the oven set-point temperature. This increases the rate of oxidation near the oven ends and allows for a longer overall particle residence time inside the heated length.

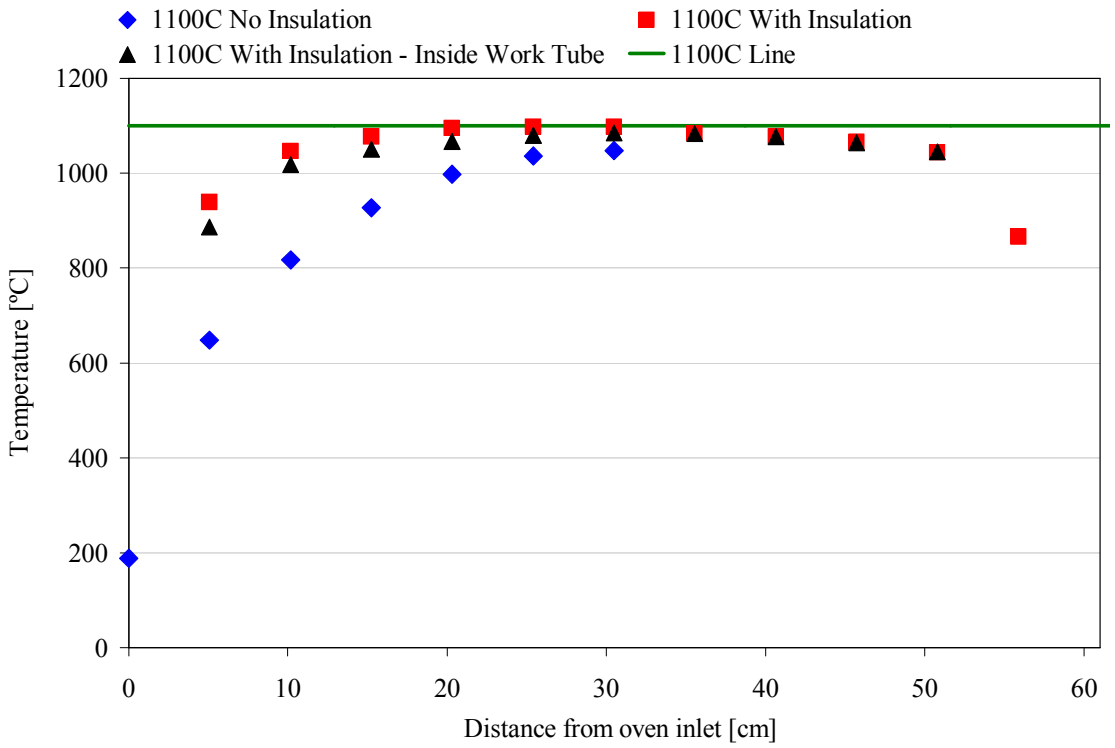

Figure 9: Temperature profile of outer wall and inside 16.7 mm ID quartz work tube inside Carbolite tube oven with and without insulated oven outlets for an oven set point temperature of 1100ºC and a 1 L/min flow rate.

The temperature inside the work tube approaches the temperatures outside of the work tube in the central heated section except very near the oven inlet and outlet. The near-constant radial temperature distribution allowed for the real-time monitoring of temperatures during sampling without having to position thermocouples inside of the work tube which would disrupt the sample aerosol. Subsequently, three thermocouples were cemented to the outside of the work tube at the midpoint of the oven and near each end. The thermocouples ultimately allow for the monitoring of oven temperature stability and actual oven temperature, potentially improving HTOM repeatability by verifying a portion of the temperature profile.

As previously noted part of the purpose of this work was to improve the HTOM apparatus and validate the measurements. Issues addressed were particle loss, low signal-to-noise ratio, sufficient oxidation of carbon, and repeatability. The apparatus represented in Figure 10 (Filice et al., 2007) was modified to minimize particle loss and increase residence time inside the oven. The coiled heat exchanger was removed to minimize diffusion losses and replaced by a short length of straight stainless tube. It was experimentally found that the coiled heat exchanger was not necessary to cool the sample to temperatures that were compatible with sampling lines and instrumentation. The quartz oven tube was changed to a 19 mm outer diameter (17 mm inner diameter) tube in an attempt to increase particle residence time at oven set point temperatures to enhance the oxidation process. The oven flow rate was lowered to 1 L/min to further increase oven residence times. The heated length residence time for the updated oven apparatus at a flow of 1 L/min was 1.4 s, over 7 times longer than that used by Kim (2005). The ejector diluter was also moved to control the flow of the aerosol following the atomizer, while the oven flow was controlled by the instrument sample flow rate. This also allowed for ease of taking up and downstream oven measurements. The dryer chamber was also switched from silica gel to activated carbon for volatile fraction removal.

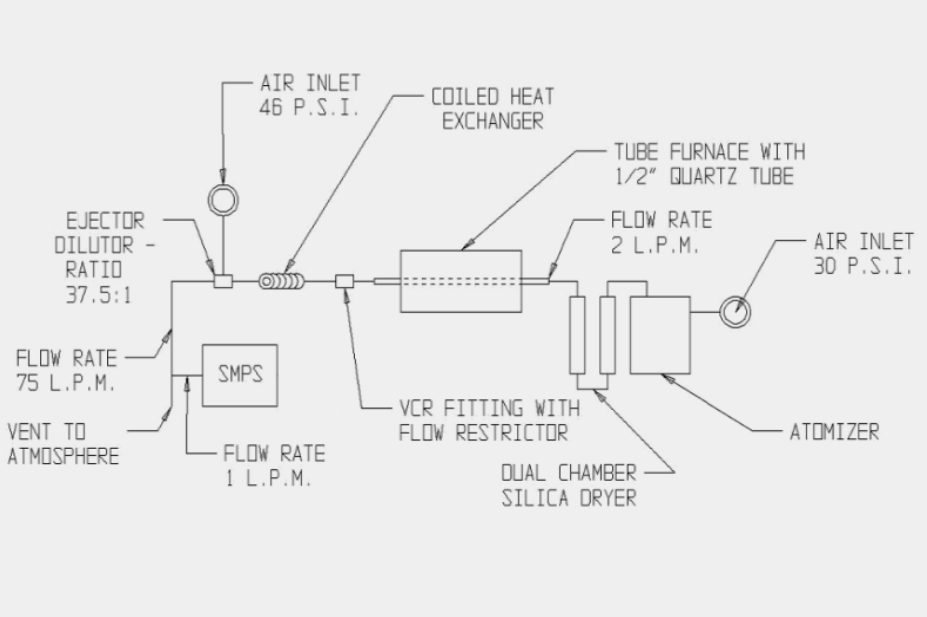

Figure 10: Schematic of HTOM apparatus that was used for Filice et al., (2007)

Other improvements were made to increase the quality and repeatability of the measurement. An oven sample flow rate of 1 L/min was used to keep a consistent and sufficient oven residence time. An effort was made to keep the upstream and downstream dilution ratios the same and constant and within an acceptable concentration range for the aerosol instruments. This strategy minimized errors caused by using multiple dilution ratios, but lowered the downstream oven concentrations necessitating modification of the sampling methods to increase the sensitivity of the SMPS measurements. By lengthening the SMPS scan time and using wider particle size bins (8 or 16 channels per decade rather than 32) some signal noise is removed. However, the distribution loses some size resolution. Ash measurement experiments using atomized lube oil and steady-state engine exhaust were conducted to evaluate these changes and are discussed in the sections that discuss the results from the lube oil spray and steady-state engine experiments.

2.3 Particle measurements: instrumentation

An integral part of the HTOM is the collection of aerosol size distribution and number concentration data up and down stream of the tube oven. The scanning mobility particle sizer (SMPS) was used for making a majority of the measurements. The SMPS is capable of making near real-time particle size distribution measurements. It is composed of two separate instruments; a differential mobility analyzer (DMA) and a CPC. Further details of the SMPS are shown in Appendix B. Other aerosol instruments used for measuring exhaust particle number weighted size distributions include a TSI Engine Exhaust Particle Sizer (EEPS) (Johnson et al., 2004) and a Cambustion DMS (Kingsley et al., 2002). Both use electrical mobility analysis to construct particle size distributions. These instruments have faster responses than the SMPS, but are not able to match the SMPS in resolution or in measuring the very low concentrations that are seen when making ash measurements. A TSI Electrical Aerosol Dectector (EAD) and a stand-alone CPC were used to measure real-time particle diameter and number concentrations respectively. They are described in more detail in Appendix A.

2.4 Atomized lube oil apparatus and procedure

Atomized lube oil spray was sampled using the HTOM to evaluate the method with an ash containing aerosol similar to that of diesel exhaust but in a less complex and more controllable form. Two types of lube spray experiments were performed. The first was discussed in Apple et al., (2009) where a fresh blend of Castrol 5W-40 lube oil was compared to a sample that was removed from the sump of a 1.9 L VW TDI engine. The used oil had the equivalent of more than 2,000 km of use. Samples of both oils were analyzed using ICP-MS to detect any concentration differences of trace metals that occurred over the life of the used oil. These results were then compared to results obtained from the HTOM.

Another type of lube oil spray test used five specially blended lube oils provided by BP-Castrol. Each blend featured the same base stock and different specific combination of lube oil additives with one blend containing no additives. Table 3 shows

the composition of the specially blended lube oil samples. A more detailed composition of the lube oil blends is shown in the Appendix A.

Table 3: Concentrations in ppm of ash related elements in specially blended lube oils

	Base stock 104A	101A	100A	103A	102A
B	<5	<5	<5	285	<5
Ca	<2	<2	3946	<2	3724
Mg	<2	<2	8	~500	<2
P	2	976	1052	<10	13
S	55	1998	802	57	8804
Zn	<5	1008	<5	<5	<5

For each lube oil spray experiment a pneumatic nebulizer or atomizer shown in Figure 11 was used to atomize mixtures of lube oil that were diluted 100:1 with butanol. Hinds (1999) gives an overview of atomization of liquids and May (1973) gives a description of the Collison type nebulizer that was used for this project. A compressed air source forces air through a small channel creating a high velocity. The high velocity channel is ported to the end of a capillary tube that is partially submersed in a fluid. The fluid is drawn up the capillary tube due to the low pressure created by the high velocity jet. The fluid is then atomized by the air jet into the container. Some of the fluid collects on the walls of the container and is re-entrained into the fluid reservoir, while the rest of the aerosol exits through a port on the top of the container.

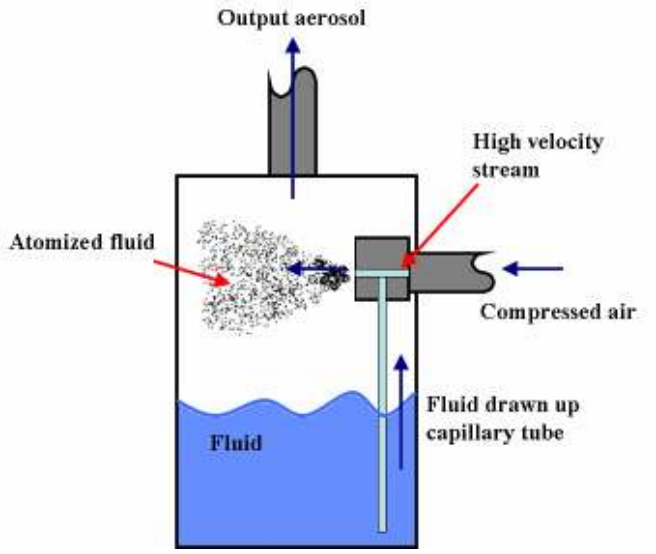

Figure 11: Diagram of nebulizer used for lube oil spray experiments

Figure 12 displays the schematic of the apparatus used during the evaluation of the HTOM for sampling specially blended lube oil aerosols. After atomization a portion of the aerosol was passed through an activated carbon scrubber to remove the butanol vapors and light hydrocarbons. The carbon scrubber contains a bed of porous carbon. The volatile vapors diffuse to the surface of the carbon and attach to the exposed carbon surface. Ideally, the aerosol exiting the carbon scrubber is a complete lube oil aerosol with only the butanol removed. This assumption is discussed later in the results section. The rest of the aerosol was vented to the atmosphere. A two-stage ejector diluter system was used to drive the flow of the aerosol through the scrubber and provide dilution.

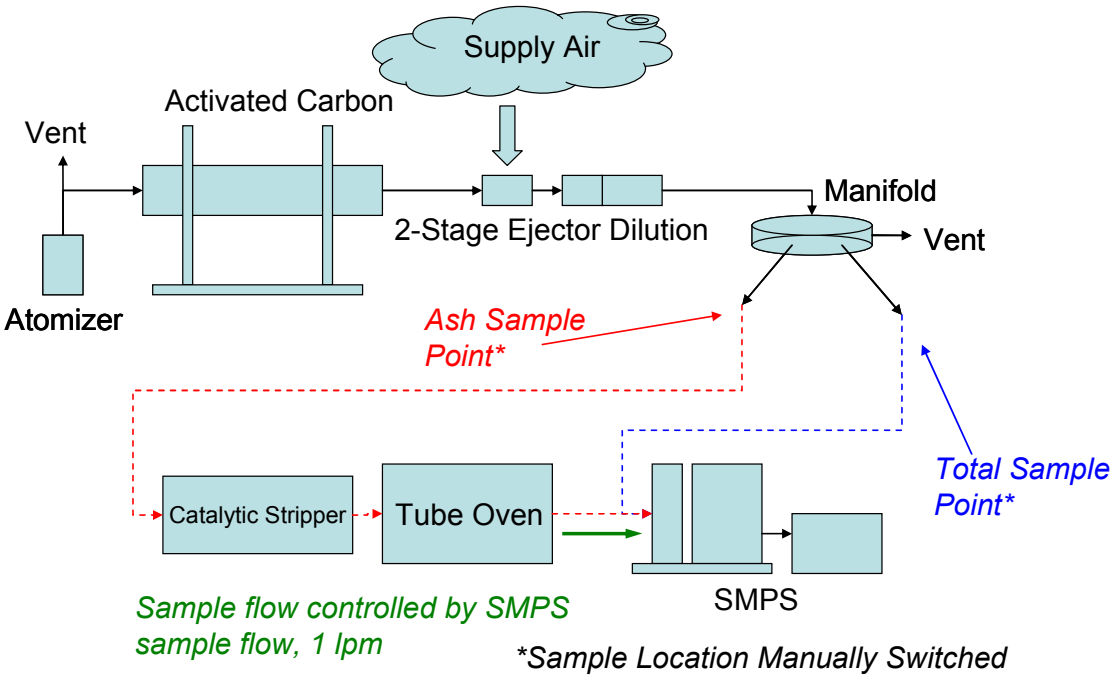

Figure 12: Schematic of HTOM apparatus used for specially blended lube oil spray experiments

After the carbon scrubber, the aerosol was treated with a heated catalytic stripper (CS) (Abdul-Khalek, 1996) and a high temperature tube oven. The CS consisted of a Pt coated catalyst heated to about 300 °C and was used as a precautionary measure to prevent possible explosions caused by sending a hydrocarbon and oxygen rich aerosol through the high temperature tube oven. The tube oven consisted of a heated cylinder with open ends. A quartz tube was used to contain the aerosol while it was passed through the oven. The tube oven's temperature ranged from ambient to 1200 °C. Particle measurements were taken up and downstream of the oven to establish a non-combustible or ash fraction.

Flow through the CS and oven was provided by the internal pump of the SMPS CPC at 1 L/min. The dilution ratio was determined by taking flow measurements of the sample flow and the total flow. Flows were calibrated at the beginning of the experiment and checked at the middle and end of the test. After dilution the sample aerosol passed through a sampling manifold where multiple instruments could be connected, and excess flow was vented to the atmosphere. Samples were taken upstream and downstream of the

CS-oven combination by switching the sample line location represented by the dotted lines in Figure 12 and by using two SMPS's.

The oven was ramped from ambient to 1100 °C. At each temperature the oven was allowed to reach the set point and then allowed to stabilize for at least 10 min. Thermocouples cemented at three axial positions on the outside of the quartz tube were used to determine oven temperature stability after temperatures were changed. Following the stabilization, up and downstream CS-oven measurements were taken with an SMPS. This procedure was completed for different fresh and used commercially available lube oils as well as the lube oil blends shown in Table 3.

2.5 Engine exhaust sampling apparatus and procedure

A schematic of the sampling apparatus is shown in Figure 13. Exhaust was sampled from a 1.9 L/min VW TDI engine and a Cummins ComfortGuard auxiliary power unit (APU). For the VW engine an eddy current dynamometer was used to supply load. A bank of incandescent light bulbs supplied the load for the Cummins APU. Specific engine details are shown in Table 4. Unless otherwise noted, the engine tests were conducted using an ULSD fuel (< 15 ppm S) and API-CJ4 standard lubricating oil. An ejector vacuum pump, supplied with dried and filtered dilution air, was used to dilute the exhaust before entering the tube oven. Dilution ratios were monitored continuously by measuring NO concentrations before and after dilution. A California Analytical Instruments, Inc. 600 Series NO analyzer with a heated sample line was used for raw NO measurements. Both a Monitor Labs Inc. Model 8840 Nitrogen Oxides Analyzer or Horiba CLA-510SS NO analyzer were used for dilute NO measurements for all the engine tests presented. Before each test all gas analyzers underwent a zero and span gas calibration. The span and zero were also checked at the end of each test.

Table 4: Test engine summary

Engine	1999 Volkswagen TDI	Cummins ComfortGuard APU
Engine Type	Compression Ignition	Compression Ignition
Displacement	1.9L	0.5 L
Aspiration	Turbocharged	Naturally Aspirated
Fuel	BP-6 (6ppm Sulfur)*	B-2 ULSD Road Fuel (<15ppm Sulfur)
Lube Oil	Castrol API-CJ4	Castrol API-CJ4

*unless otherwise noted (some tests used ECD-1 ULSD (<15ppm S) and BP-50 (50ppm S) Diesel fuel

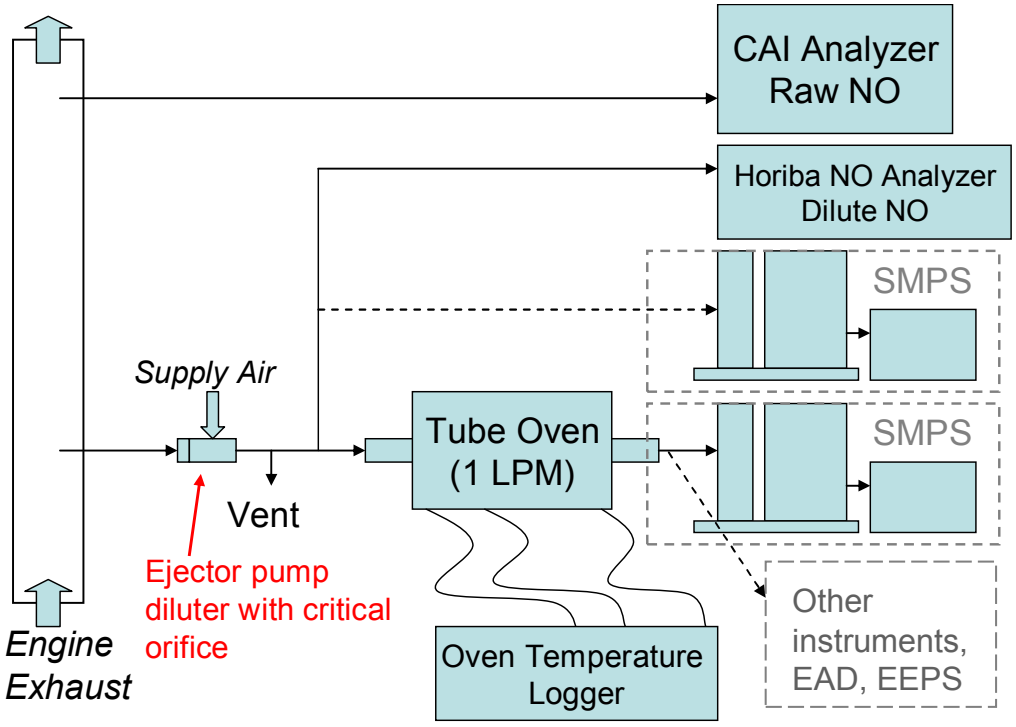

Figure 13: General schematic for engine exhaust ash sampling with the HTOM

After dilution part of the sample passed through the high temperature tube oven at 1 L/min; additional flow was vented to the atmosphere. The oven flow rate was set by the sample flowrate of the downstream particle instrument. The SMPS was used to measure the particle number size distributions which were used to calculate total number and volume concentrations. The sample line of the SMPS was switched between the upstream position to make total exhaust measurements and the downstream position to

make ash measurements. For certain experiments other instruments were used along side the SMPS such as an EEPS, stand-alone CPC, and EAD. When the downstream oven instruments required more than 1 L/min of sample flow, a filtered bypass diluter (FBD) was used. The FBD consisted of a splitting the instrument sample flow between the tube oven and a HEPA type filter open to room air. The flow was controlled using a needle valve on the tube oven flow side. The instrument(s) inlet flow was measured along with the oven inlet flow to determine the dilution ratio.

Two different tests were performed while sampling steady-state engine ash emissions: baseline and lube oil doped fuel testing. Using the specially blended lube oils described in Table 3 the lube oil doped fuel artificially increases lube oil consumption; improving the ash signal and allowing for an ash mass penetration calculation.

2.6 Ash penetration of a loading DPF apparatus and procedure

The HTOM was used to study the penetration of ash through a DPF. Measurements were taken throughout the first half-hour of the loading of a fully regenerated DPF. Both soot penetration and ash penetration were examined. The 1.9 L VW TDI engine was fitted with an aluminum titanate DPF provided by Corning. Before each test, the DPF was fully regenerated by baking in an oven above 600°C for at least 2 hours. Figure 14 displays a schematic of the engine and sampling apparatus. Exhaust sample ports were located both up and downstream of the DPF. Samples were drawn from the exhaust by vacuum ejector pumps that provided dilution with dried and filtered air. Dilution ratios were monitored by measuring the raw and diluted NO gas concentration. Table 5 shows the measured dilution ratios.

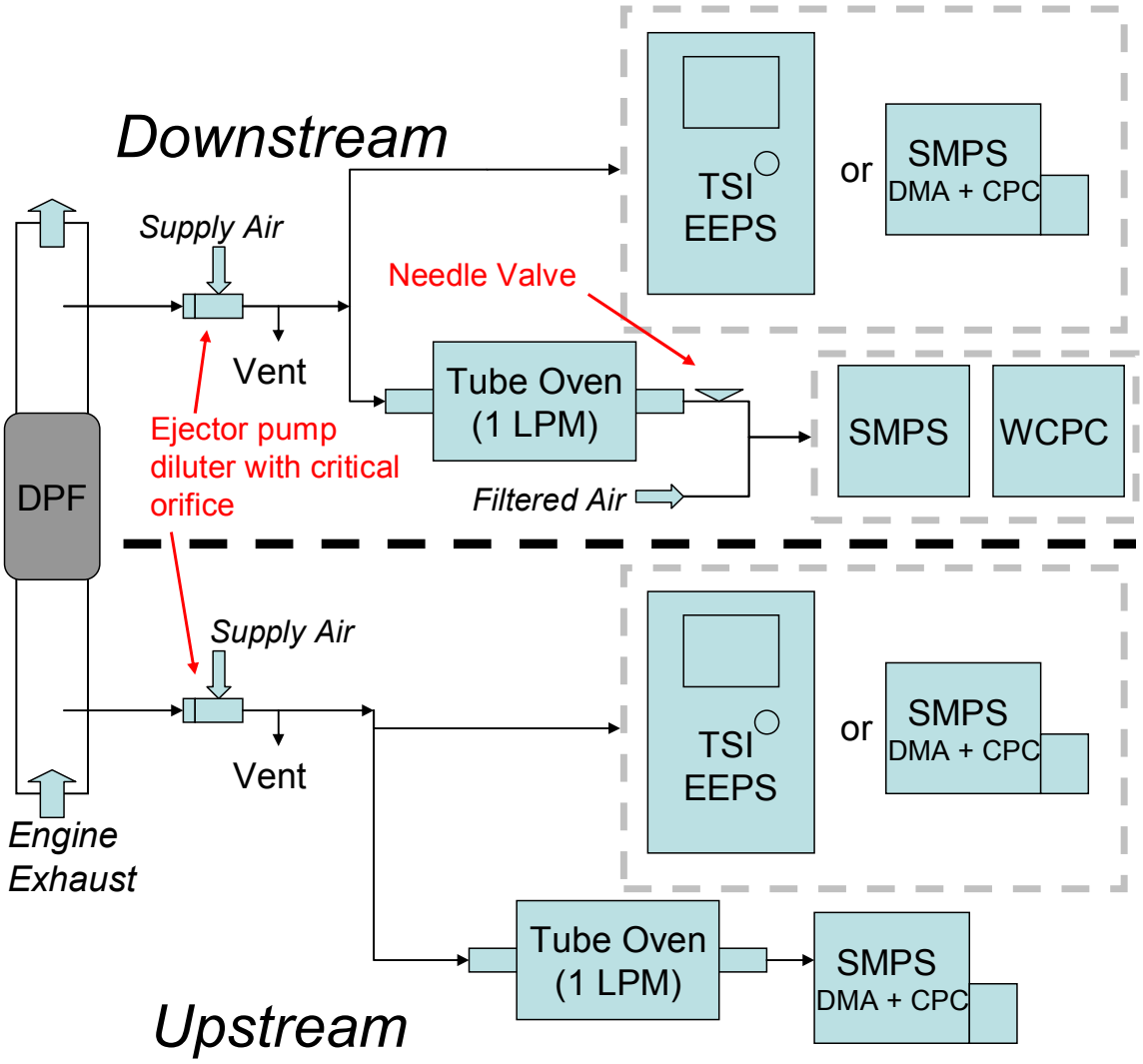

Figure 14: Schematic of apparatus used for the ash penetration of a DPF study

Table 5: Total particle and ash dilution ratios measured during downstream DPF measurements

	Dilution Ratio	
DPF Test	Total Particle	Ash
1	150:1 - 195:1	4:1
2	80:1	7:1

Total exhaust particle measurements were made after the dilution stage and before the tube oven using a TSI Engine Exhaust Particle Sizer (EEPS) for the first test and a

TSI Scanning Mobility Particle Sizer (SMPS) for the second test. These instruments measure number-weighted particle size distributions measurements. The particle instrument pumps, located downstream of the oven, pull sample air through the oven at a flow rate of 1 L/min. When instruments required more than 1 L/min, a filtered bypass flow was used with the oven flow set by a needle valve. A correction was made for the dilution provided by the filtered bypass flow. Another SMPS was used to measure the ash size distributions downstream of the oven, and a TSI 3782 water based condensation particle counter (WCPC) was used to monitor real-time total ash particle number concentrations. The oven was set to 1100 °C.

2.7 Particle measurement: loss mechanisms

To fully understand measurements made using the HTOM, an understanding of the physical system is crucial. The HTOM alters an already complex aerosol such as engine exhaust by exposing it to temperatures of up to 1200 ºC. Particle measurement techniques are then used to quantify the multifaceted aerosol in real or near real-time. To more accurately interpret the particle measurements; the fundamental particle mechanics of the system must be understood. For instance, two major particle loss mechanisms of concern are diffusion and thermophoresis.

Diffusion is caused by concentration gradients. Equation 1 displays the particle flux J as described by Fick's first law of diffusion, given in terms of the diffusion coefficient D and the concentration gradient dn/dx (Hinds, 1999).

$$J = -D\frac{dn}{dx} \tag{1}$$

The diffusion coefficient is shown in Equation 2 in terms of the Boltzman's constant k, absolute temperature T, slip correction factor C_c, gas viscosity η, and particle diameter d_p. This can also be simplified as shown in Equation 3 by substituting in the particle mobility B.

$$D = \frac{kTC_c}{3\pi\eta d_p} \tag{2}$$

$$D = kTB \tag{3}$$

Aerosol particles tend to adhere to surfaces when they collide, effectively removing particles from the aerosol and reducing the particle number concentration. By understanding the mechanisms surrounding diffusion, losses in particle sampling lines can be predicted. Using the dimensionless deposition parameter μ defined in Equation 4, numerical solutions for particle penetration through a cylindrical tube can be used. Numerical solutions shown in equations 5 and 6 were arrived at for two different ranges of μ (Baron and Willeke 2001). The small μ value equation was referenced from Gormley and Kennedy (1949) and Newman (1969).

$$\mu = \frac{\pi D L}{Q} \tag{4}$$

$$P = 0.81905e^{-3.6568\mu} + 0.09753e^{-22.305\mu} + 0.0325e^{-56.961\mu} + 0.01544e^{-107.62\mu} \text{ for } \mu > 0.02 \tag{5}$$

$$P = 1.0 - 2.5638\mu^{2/3} + 1.2\mu + 0.1767\mu^{4/3} \text{ for } \mu \leq 0.02 \tag{6}$$

Figure 15 displays the calculated particle penetration versus spherical particle diameter through the tube oven used in the HTOM at two different temperatures assuming a tube length of 46 cm and a constant flowrate of 1 L/min at 300 K. It shows that although diffusion increases with temperature, the increased flowrate causes a higher particle penetration at 1100 °C. The model shows particles larger than 10 nm have penetrations efficiencies of > 70 %. The curves emphasize the importance for size specific corrections when compensating for diffusion losses while making particle measurements. However, for this project particles much less than 10 nm in diameter were not in the measurement range of the instrumentation.

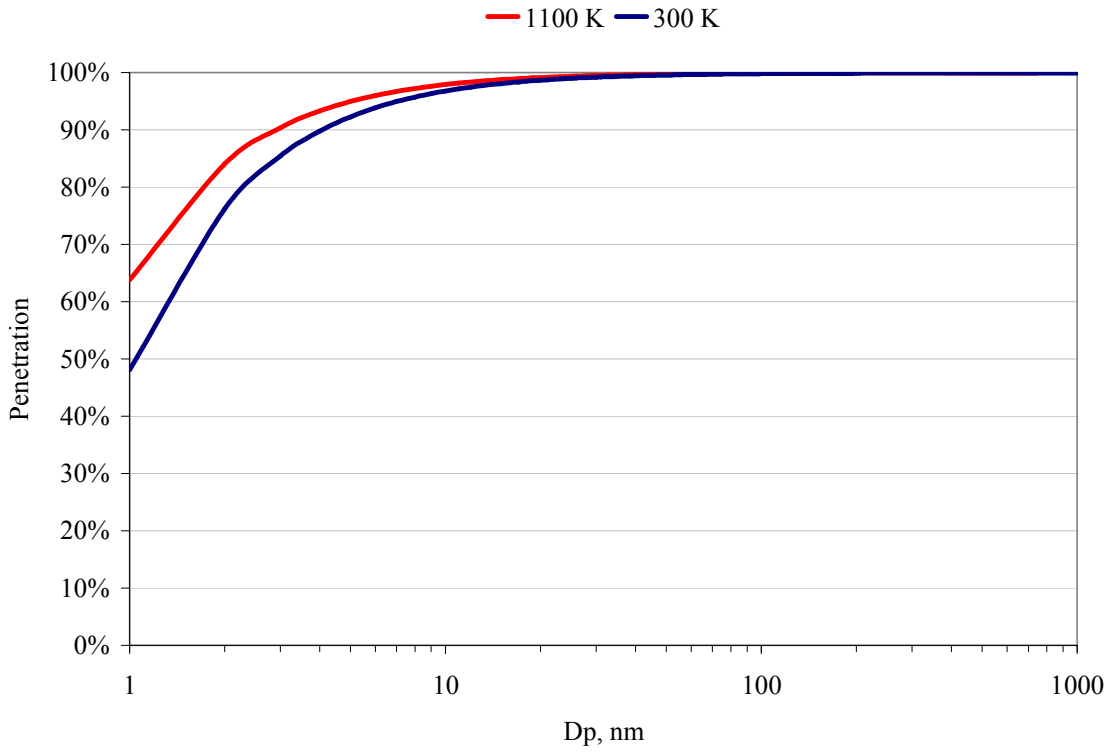

Figure 15: Spherical particle penetration versus particle diameter based on diffusion through a cylindrical tube at two different temperatures

Thermophoresis is the phenomenon where a particle experiences a net force in the direction of a lower temperature (Hinds, 1999). Thermophoretic forces are caused by the molecules colliding with the particle having different average velocities on opposite sides of the particle. Thermophoretic losses occur when sample lines contain aerosols of higher temperature than the surroundings. The impact of thermophoresis can be significant for temperature gradients in the region of 50 K/cm as reviewed in Walker et al., (1979) and studied experimentally in Fulford et al. (1971), Derjaguin et al. (1993), and Goldsmith et al. (1966). Equation 7 gives the thermophoretic particle number penetration in a tube as a function of the temperature ratio raised to the product of the Prantl number and K_t. Appendix B shows a more detailed derivation of this equation.

$$\left(\frac{n_o}{n_i}\right)=\left(\frac{T_o}{Ti}\right)^{\Pr K_t} \tag{7}$$

Equation was used to correct for thermophoresis in the following data unless otherwise noted. Oven tube diffusion corrections are more difficult to implement due to the transient nature of the reacting aerosol. Thermophoretic forces most likely minimize diffusion losses in the first portion of the oven during the heating of the aerosol. These losses probably begin in the final segment of the oven. Because of this, particle penetration based on diffusion is likely greater than that shown in Figure 15. Internal oven diffusion losses were not made. Diffusion losses in the SMPS were performed internally by the TSI AIM software.

2.8 Particle measurement: methods

The data from each SMPS particle size distribution is divided into particle size bins. These bins were in the form of $dN/d\log D_p$ where dN is the number of particles per bin and $d\log D_p$ was the width of the bin. Total particle concentrations can be calculated by integrating the size distribution as shown for number concentration (N) in Equation 8.

$$N=\sum\left(\left(\frac{dN}{d\log D_p}\right)\left(d\log D_p\right)\right) \tag{8}$$

The number weighted distribution can also be weighted for particle diameter, surface area, volume, and mass by multiplying each particle bin by a geometric factor containing the mean particle diameter of the specific bin. Equation 9 shows the particle volume (V_p) calculation assuming spherical particles. Particle mass (m_p) can be calculated by multiplying V_p by the density. Equation 10 shows the subsequent calculation for total volume concentration (V).

$$V_p=\frac{\pi D_p^{\,3}}{6} \tag{9}$$

$$V = \sum \left(\left(\frac{dV}{d \log D_p} \right) \left(d \log D_p \right) \right) \tag{10}$$

It should be emphasized that these calculations were made based on the assumption of spherical particles using particle mobility diameter measurements. The ash particles appeared to be spherical in shape as shown in Figure 16. However, soot particles are typically chain-like agglomerates formed by spherical primary particles. An example of a soot particle is shown in Figure 3. The agglomerate nature of soot particles will cause some error when calculating particle volume and mass from mobility diameter measurements. Park et al. (2003) shows the relationship between mobility and mass for Diesel exhaust particles.

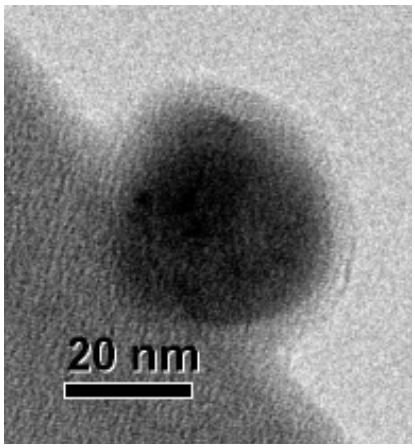

Figure 16: TEM image of ash particle from atomized 100A (Mg/B) blend lube oil sampled downstream of 1100 °C tube oven

For each steady-state test completed (lube spray and engine exhaust) the temperature of complete oxidation was determined as described in the subsequent paragraphs. Total particle number and volume concentrations were calculated from SMPS measurements taken downstream of the tube oven at stabilized oven temperatures. Temperatures included room temperature and at 200 ºC intervals from 300 to 1100 ºC. At each oven temperature the total particle fraction penetrating the oven was calculated downstream and upstream by dividing the downstream concentration by the upstream concentration. The volume fraction (F_V) and number fraction (F_N) are shown in

Equations 11 and 12 respectively.

$$F_V = \frac{V_{Downsream}}{V_{upstream}} \tag{11}$$

$$F_N = \frac{N_{Downsream}}{N_{upstream}} \tag{12}$$

Insight into the oxidation process can be gained by plotting the volume and number fractions versus temperature as shown in Figure 17. This plot is from the atomized lube oil. Noting that the x-axis uses a log scale, it can be seen that the rate of change in volume fraction decreases with temperature. At 700 ºC and above the value is essentially unchanging. Therefore, it can be inferred that full oxidation has occurred and the remaining particles are a fairly stable metallic compound. 1100 ºC was chosen as the oven temperature to make a majority of the ash measurements using lube oil spray.

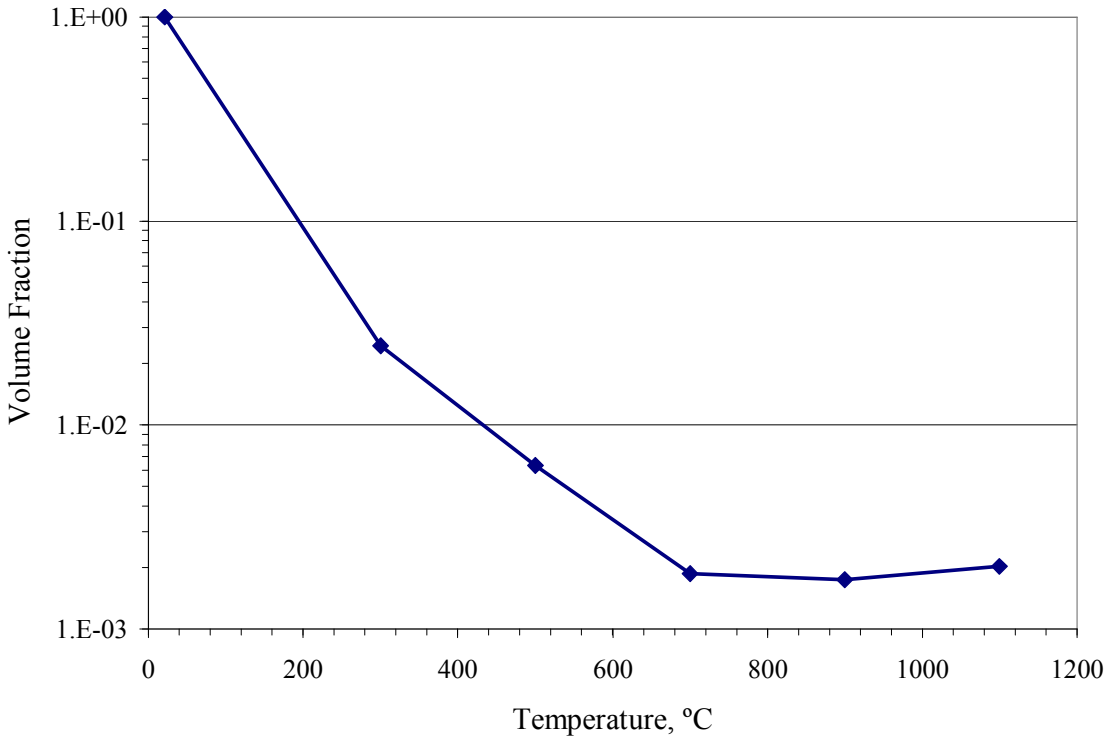

Figure 17: Particle volume fraction penetrating tube oven versus oven set temperature (from atomized synthetic lube oil)

Equation 13 shows the ash volume fraction relating to the mass fraction if the particle densities are known or assumed. Assuming that the carbon scrubber in the apparatus removes all the volatile butanol vapors, only the complete atomized oil remain. For all calculations 0.85 g/cm^3 was used for an oil density because it falls within the range of oil densities that are commonly used in on-road applications (Gligorijevic et al., 2006). Based on previously explained rationale, the remaining aerosol downstream the 1100 ºC oven is assumed to be composed entirely of metallic ash. The ash particle densities varied based on lube oil additive composition.

$$F_m = \frac{\rho_{ash} V_{ash}}{\rho_{oil} V_{oil}} = \frac{\rho_{ash}}{\rho_{oil}} F_V \tag{13}$$

2.9 Chemical equilibrium analysis

To better understand the chemistry involved with metallic lube oil additives at the high oven temperatures chemical equilibrium modeling was conducted using NASA Chemical Equilibrium with Applications (CEA) software. NASA CEA calculates chemical equilibrium compositions and properties of complex mixtures using independent databases with thermodynamic and transport properties of chemical species (McBride and Gordon, 1992; Gordon and McBride, 1994; Zehe et al., 2002).

Chemical equilibrium modeling was completed for each of the specially blended lube oil additive packages detailed in Table 3. The modeling consisted of known metallic compounds with similar elemental composition to the additive blends. It was not completed for the specific chemical compounds contained in the additive because these data are not available in the equilibrium model. It is expected, however, that the modeled compounds are representative equilibrium products. The one concern is that kinetics may limit the formation of the equilibrium products especially at lower temperatures. Baseline lube oil spray volume concentrations measured by the SMPS and the known additive concentrations were used to find the additive elemental concentrations for the equilibrium models.

Figure 18 through Figure 21 show the results from the chemical equilibrium modeling. The elemental composition of the additive package for each known lube oil blend was taken into account when selecting the input elements for the model. The trace elements in the base stock or 104A blend, is not shown due to the very low additive concentrations.

Figure 18 and Figure 19 show the equilibrium model results for blends 100A (Ca/P/S) and 102A (Ca/S). Both display a higher mole fraction of Ca based molecules and a stable CaO at high oven temperatures. The higher sulfur content of blend 102A (Ca/S) suppresses the formation of $CaCO_3$ at lower temperatures.

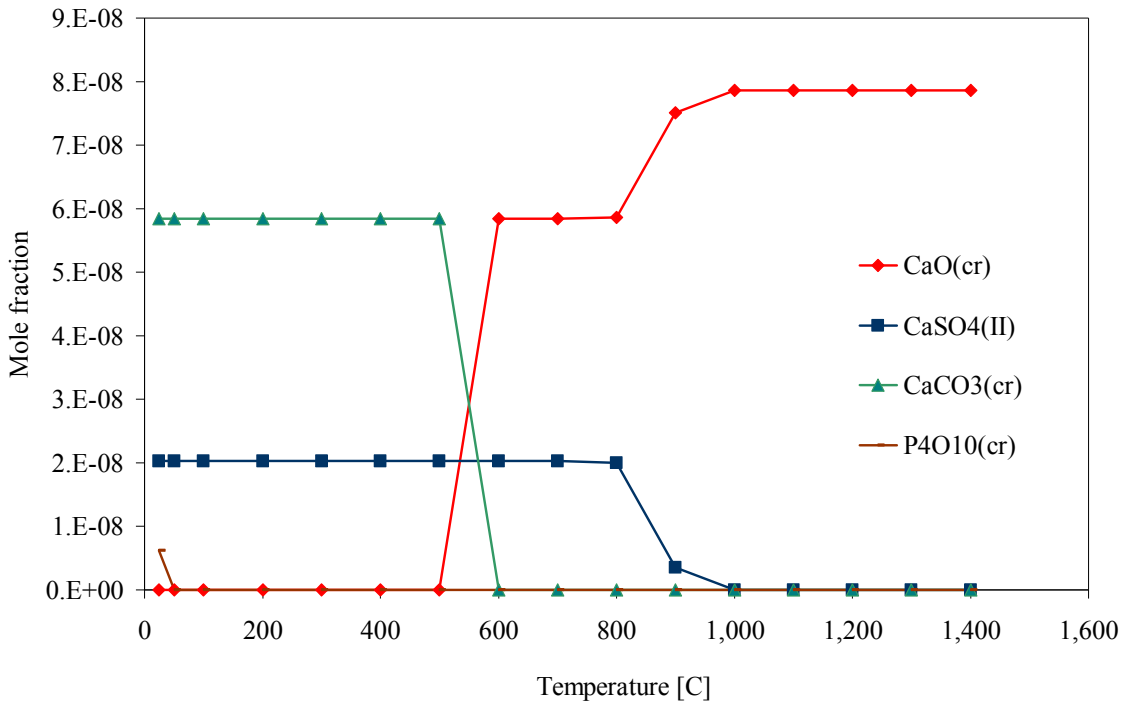

Figure 18: Chemical equilibrium model versus temperature for oil blend 100A (Ca/P/S) (solid compounds shown)

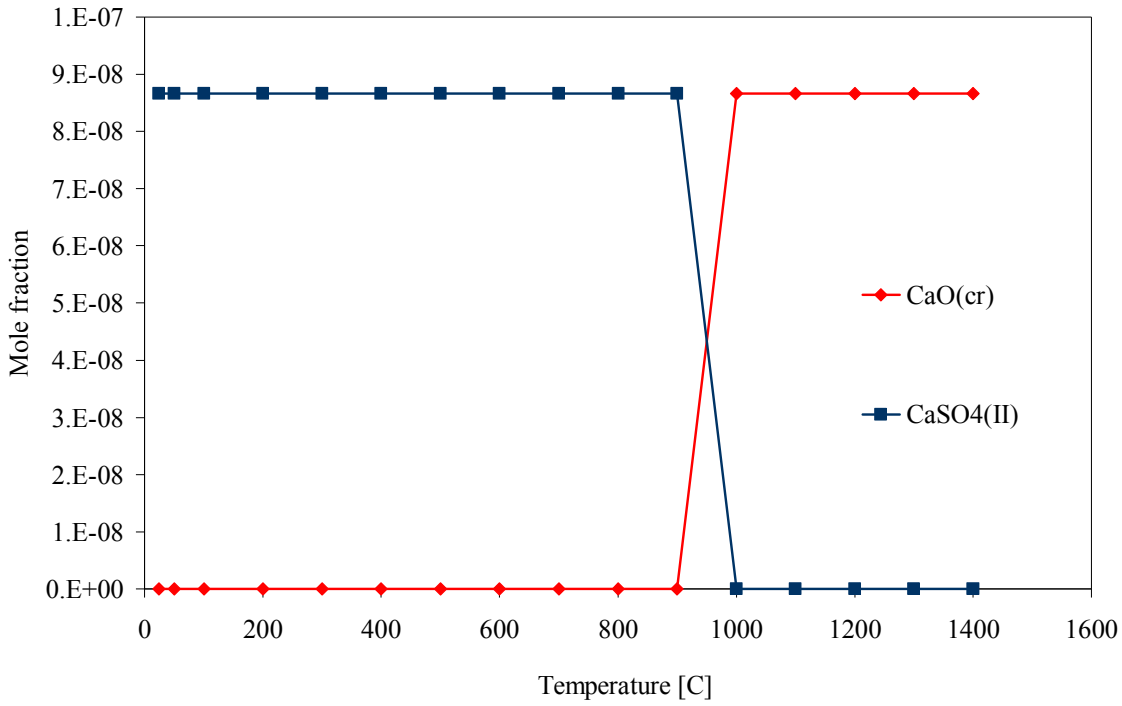

Figure 19: Chemical equilibrium model versus temperature for oil blend 102A (Ca/S)

Blend 101A (Zn/S/P) contained an additive package consisting mostly of Zn, P, and S. Based on the equilibrium model shown in Figure 20, S generally stays in a gaseous form especially at higher temperatures. The Zn is shown to be in a solid sulfate form up to 700ºC before it changes to a gaseous elemental form at higher temperatures. The model shows a fairly stable $ZnSO_4$ until 700ºC. The Zn in Blend 101A is most likely in the form of a Zn dithiophosphate (ZDDP) which is designed to form anti-wear coating on internal engine surfaces at engine operating temperatures. ZDDP was not in the thermodynamic library used by the NASA CEA software; therefore Zn, P, and S were inserted into the model as individual elements in their specific elemental concentrations. Zn phosphate has been reported in engine exhaust but the thermodynamic library did not contain any Zn/P compounds.

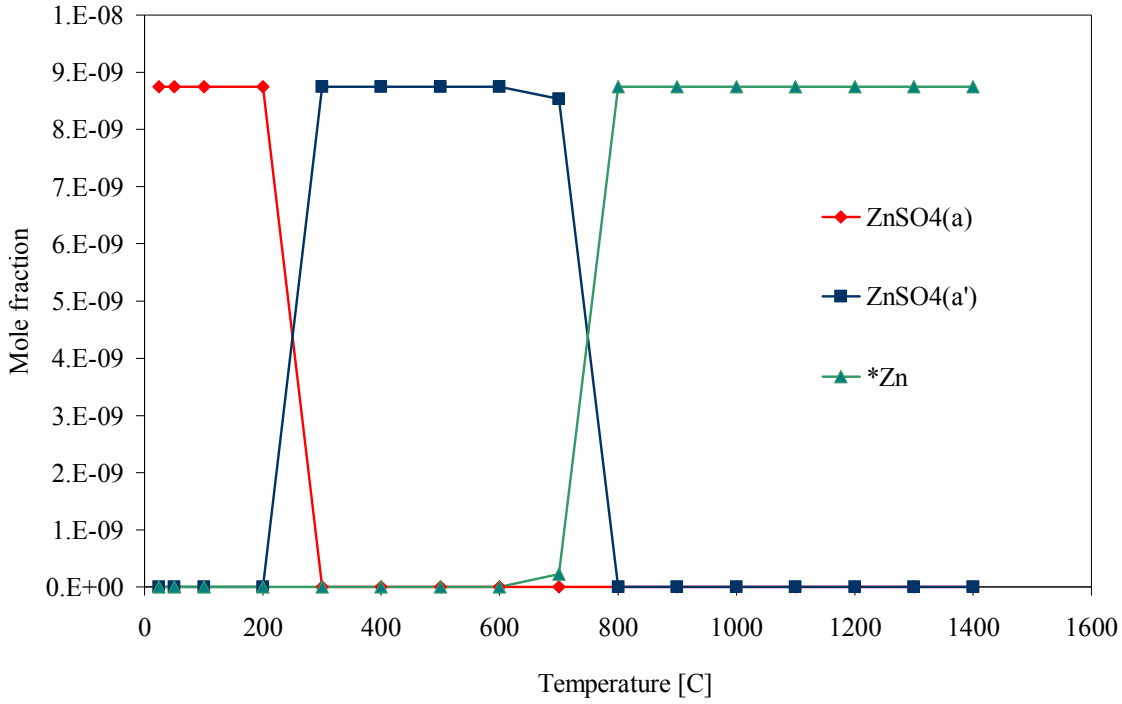

Figure 20: Chemical equilibrium model versus temperature for oil blend 3 (Zn, S, and P)

Figure 21 displays the chemical equilibrium model for blend 103A (Mg/B). The equilibrium model shows that Mg quickly forms MgO solids and is very stable, especially at temperatures above 600ºC. The B, however, changes from a crystal to a liquid after 400ºC. The liquid then turns to a gaseous form around 800ºC.

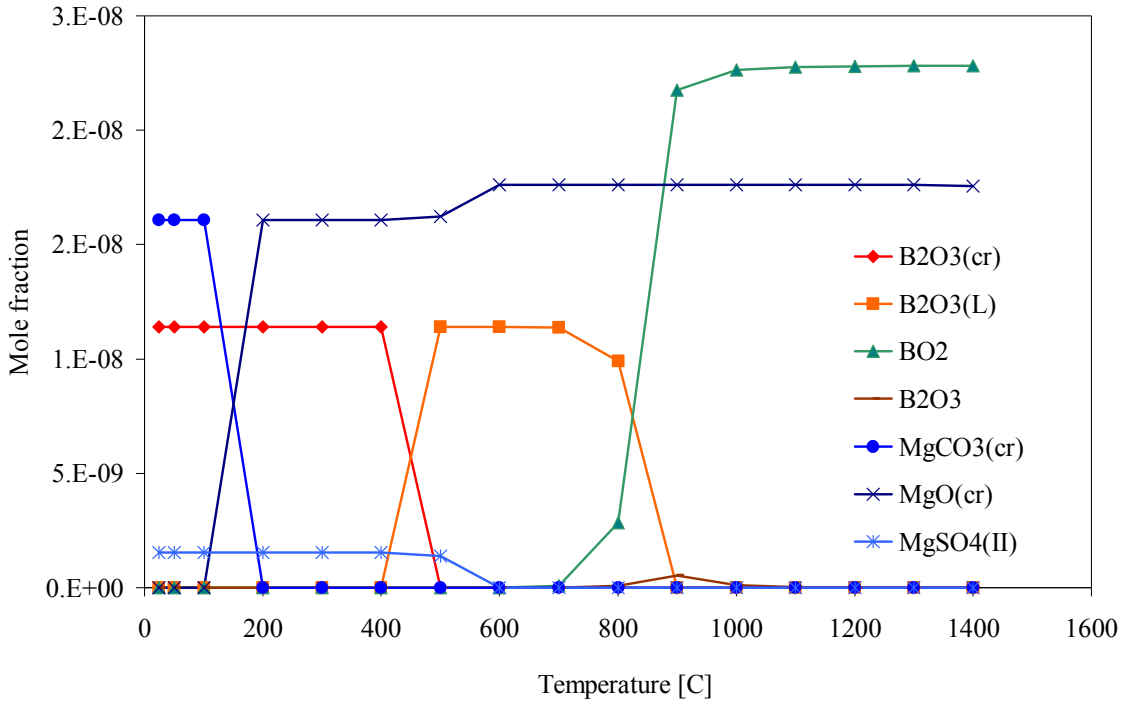

Figure 21: Chemical equilibrium model versus temperature for oil blend 5 (B and Mg)

Chapter 3: Atomized lube oil results and discussion

The HTOM was used to determine the ash content of several blends of atomized lubricating oil. As mentioned earlier, this was used to validate the performance of the HTOM with types of ash that were similar to Diesel engine exhaust ash but in a simpler and more stable aerosol. It was also used to determine the sensitivity of the HTOM so specific elements and compounds used as oil additives.

3.1 Used and fresh lube oil comparison

Samples of fresh and used Castrol VW lube oil were analyzed. The used lube oil was taken from the sump of a 1.9 L VW TDI engine. Figure 22 shows the number weighted size distributions for the fresh and used lube oil sprays at oven temperatures of 25, 500, and 1100 ºC. The baseline distributions are similar, showing that a majority of particles are greater than 30 nm. At an oven temperature of 500 ºC, the accumulation mode (> 30 nm) diminishes which coincides with the appearance of a large nucleation mode peaking near $1x10^9$ part/cm. The nucleation mode (< 30 nm) peak suggests that aerosol is fractioning or evaporating in the oven and then re-nucleating downstream. The fresh and used oil size distributions appear slightly bimodal at 500 ºC with a prominent peak at around 10 and 14 nm for the used and fresh oils respectively. The difference could be attributed to more volatile components in the fresh oil and slightly different concentrations of ash forming metals in the oils due to the non-uniform nature of oil consumption (Givens et al., 2003). For oven temperatures of 700ºC and above, the nucleation mode was diminished by over an order of magnitude from the 500 ºC distribution. This is shown with the 1100 ºC distributions. The removal of the large nucleation mode peak suggests complete oxidation of all evaporated volatiles that were shown to re-nucleate after lower temperature treatments.

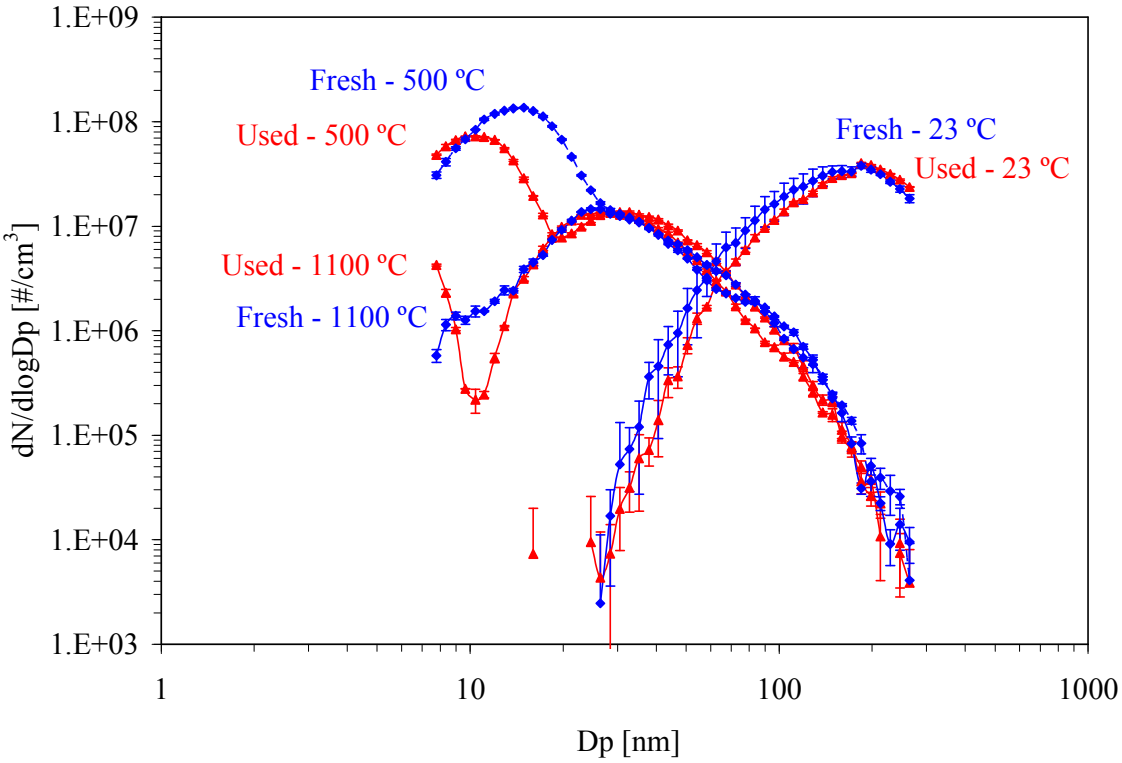

Figure 22: Number weighted size distributions for fresh and used Castrol VW lube oil sprays
(Note: corrected for dilution and thermophoretic losses; error bars represent the standard deviation of at least three samples)

Figure 23 shows both the particle number and volume fraction penetrating the tube oven for the fresh and used lube oils. The number fractions follow the trends depicted in the size distributions in that at 500 ºC there is a large spike in total number, sometimes up to an order of magnitude greater than the upstream most likely due to re-nucleation of particles downstream the oven. This spike is followed by a decrease that stays fairly constant above 700 ºC at around 0.4. The used Castrol oils show a convergence in number fraction remaining at 900ºC and 1100ºC.

The volume fraction trends show the same difference between the synthetic and Castrol oils at 500 ºC. The fresh Castrol oil showed a remaining ash volume fraction of around 1.0 %.

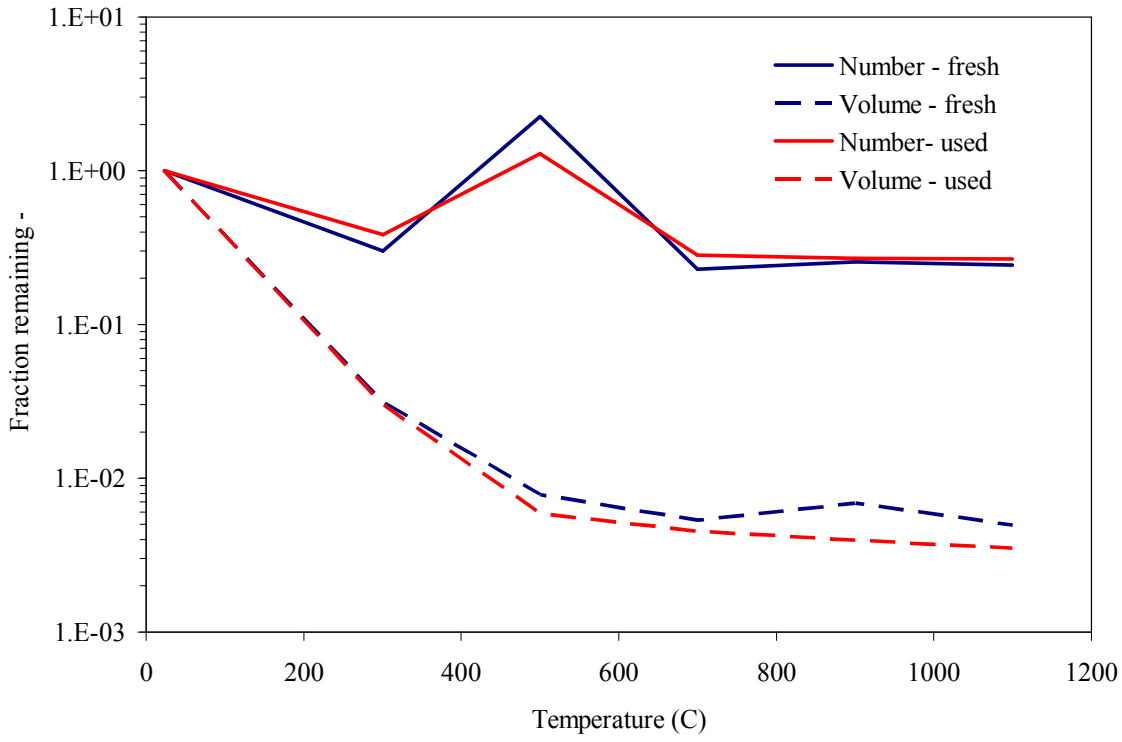

Figure 23: Volume fraction penetrating oven for used and fresh Castrol VW lube oil sprays

Table 6 shows ICP-MS results for metallic ash related element concentrations in the fresh and used Castrol lube oils. ICP-MS detectability limits for the elements of interest are shown in Appendix C and are much lower than the measured changes.

Table 7 shows typical used lube oil trace metal composition. Table 6 shows an 194 % increase in Fe from fresh to used lube oil. The Fe increase is most likely due to engine wear from abrasion of the cylinder liner or piston (Okada et al., 2003). Results showed expected quantities of Ca in both samples, with it being the most abundant metallic species. Ca decreased by 3.8 % from fresh sample to used sample. Non-uniform oil consumption could explain the decrease in Ca and S concentrations (Wahiduzzaman et al., 1992). Cu, Pb, and Sn are usually indicators of bearing wear and showed no measurable change in concentration. Cr which can come from coolant leaks or chromed piston ring wear showed no change in concentration either. There was a small increase in Si which was most likely negligible. Si increases can come from ingested dust and

sometimes piston wear (Caines and Haycock, 1996). An increase in B occurred, which was slightly above typical levels. Boron is a common lube oil additive, but is also found in some coolant and could be a sign of slight coolant contamination (Caines and Haycock, 1996). Mg increased by 1.66 times in concentration between the fresh and used lube oils. It can be found in engine components and as a lube oil additive (Caines and Haycock, 1996). The Mg increase could be a sign of engine wear. Ca, P, and S all changed less than 11 %. In total there was a slight decrease in ash related constituents with 6 elements increasing in concentration and 2 decreasing.

Table 6: ICP-MS results for ash related constituents in used and fresh lube oil samples

Elements by ICP	Fresh ppm	Used ppm	Change ppm	% difference
Ca	2996	2884	-112	-3.8%
Mg	10	106	96	165.5%
P	899	918	19	2.1%
S	4871	4529	-342	-7.3%
Zn	963	1073	110	10.8%
B	<5	20	NA	NA
Fe	1	68	67	194.2%
Si	3	5	2	50.0%
Na	11	12	1	8.7%

Table 7: Typical trace metal analysis of used oils from medium/large duty engines (Caines and Haycock, 1996) (Note: Elements with measured increase not shown had no detectable change in concentration)

Element	Typical Levels ppm	Warning Level ppm
Fe	30 - 70	100
Al	10 - 20	25
Cu	15 - 25	50
Pb	20 - 40	50
Sn	2 - 10	20
Cr	2 - 10	20
Si	10 - 20	25
B	5 - 10	25

Table 8 shows the expected and measured ash mass fraction calculated for the fresh and used lube oil sprays. At 1100 ºC the remaining ash aerosol was assumed to be composed of metal oxides. Ca is a major constituent in lube oil additive packages. Chemical equilibrium modeling summarized in section 2.9 and other analysis on ash particles for this project have shown that CaO would be the stable Ca compound at 1100 ºC. Therefore, the density for CaO (3.3 g/cm^3) was selected for the particles after the high temperature treatment. The mass concentrations and remaining mass fractions were then calculated for the lube oil sprays. The used and fresh oils showed ash mass fraction of 2.4 and 3.4 % respectively. The expected ash mass fractions were also calculated based on ICP-MS analysis of the lube oils. Based on the composition and concentration of ash species, the oil ash was assumed to be in the form of $CaSO_4$. In both cases, the HTOM over estimated the ash fraction of the lube oil when compared to the ICP-MS results by between 2 and 4 %.

Table 8: Metallic ash mass fraction comparison between HTOM and ICP-MS

	Mass concentration [g/cm3]	
Oven Temperature	Fresh Castrol VW	Used Castrol VW
25 ºC	3.5E-08	3.8E-08
1100ºC	1.2E-09	9.2E-10
	Ash fraction	
Measured from calc. mass	3.40E-02	2.40E-02
Expected from ICP-MS	9.80E-03	9.60E-03
Measured/expected	3.5	2.5

3.2 Specially blended lube oil

Table 9 shows results from a quantitative analysis of the repeatability of the specially blended lube spray HTOM experiments. The total ash particle number and volume fractions that penetrated the oven at 1100 °C are shown. The last two columns show the percent difference in each of the compared sets. The bold numbers represent the percent difference in a pair of experiments that both used the updated apparatus and procedure. The 100A (Ca/P/S) and 103A (Mg/B) blends were tested twice using the updated apparatus and demonstrated differences in ash volume fractions of 6.1% and 2.4%, respectively. This is a large improvement considering the differences of the other volume fractions shown range between 30 to 46%. The number fraction repeatability was also improved, showing that nucleation mode (<30 nm) particles were also repeatable. These tests demonstrate the improved performance of the updated apparatus.

Table 9: Repeatability analysis of lube oil spray experiments

				Ash/total concentration		% Difference	
Blend #	Additives [ppm/element]	Apparatus [current/old]	Date	Number fraction	Volume fraction	Number fraction	Volume fraction
	3724/Ca	old	10/30/2008	7.1E-01	5.3E-03		
102A	8804/S	current	12/2/2009	5.4E-01	7.2E-03	28.2%	30.8%
	285/B 500/Mg	old	11/2/2008	4.9E-01	5.5E-04		
103A	57/S	current	11/29/2009	2.4E-01	7.9E-04	66.8%	36.8%
	3946/Ca 1052/P	current	11/24/2009	5.6E-01	7.8E-03		
100A	802/S	current	11/30/2009	5.4E-01	7.3E-03	**4.2%**	**6.1%**
	285/B 500/Mg	current	11/29/2009	2.4E-01	7.9E-04		
103A	57/S	current	12/1/2009	2.4E-01	7.8E-04	**2.3%**	**2.4%**

repeatability of updated apparatus shown in bold

Figure 24 displays a representative volume weighted particle size distribution for each recent lube oil spray experiment measured downstream of the oven at 1100 °C (ash) and upstream of the oven (oil spray). All the results shown are from the updated apparatus. The 100A (Ca/P/S) blend shows an ash distribution and volume concentration similar to the 102A (Ca/S). The Ca containing oil spray ash distributions only significantly deviated from one another under 30 nm, where the effect on total volume concentrations is minimal. The 103A (Mg/B) blend distribution exhibits lower concentrations and smaller particles with the peak volume at about 25 nm compared to about 45 nm for the Ca blends. Above 150 nm there are several size channels where no particles were measured indicating that the measurements are at the limit of detection and subject to large uncertainties. The 101A (Zn/P/S) blend results display very low concentrations of ash particles, as shown in the volume fraction plot. The particle concentrations measured downstream of the oven with the Zn additives was low, about 5000 part/cm^3 at 1100°C. However, except for the largest particles the uncertainties in the size distributions are relatively small reflecting improvements made in the methodology.

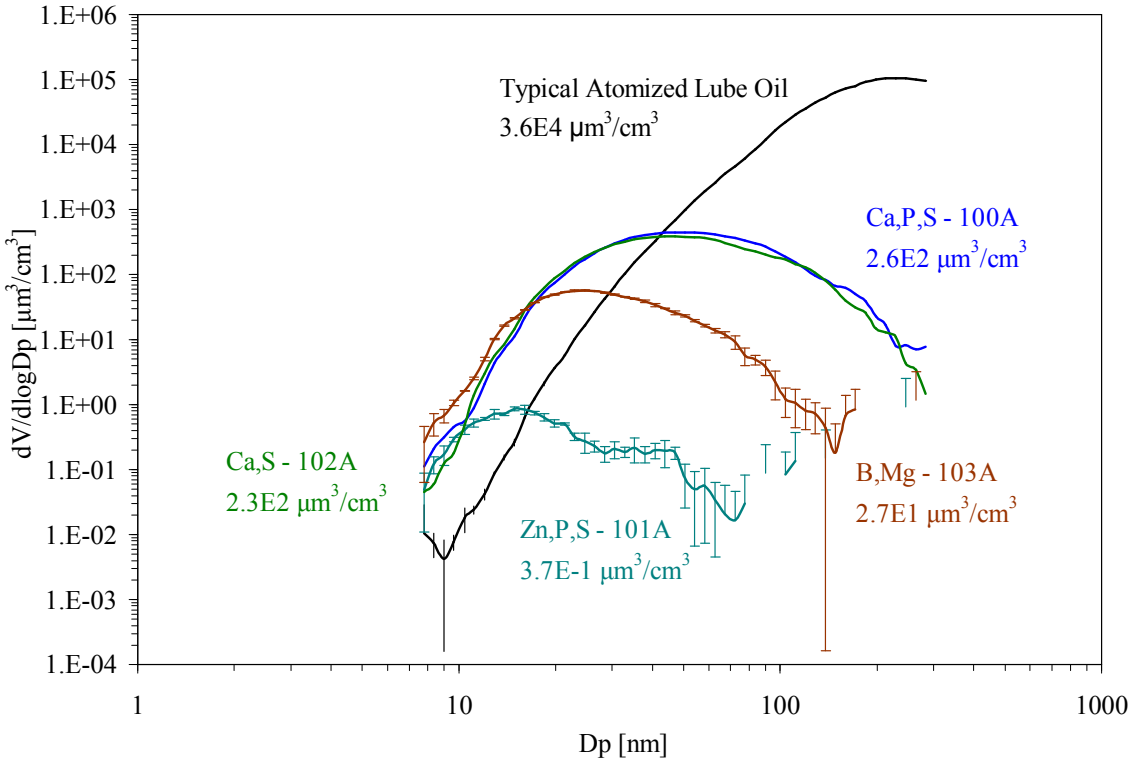

Figure 24: Average volume weighted ash particle size distributions from specially blended lube sprays
(Note: error bars represent the standard deviation of at least three samples)

Figure 25 shows the volume fraction remaining downstream of the oven over several oven temperatures for selected experiments of each lube oil blend. The 100A (Ca/P/S) oil blend shows a stable volume fraction of 0.7 to 0.8% at temperatures above 700 °C and shows good agreement with the 102A (Ca/S) oil blend which also contains Ca. The 103A (B/Mg) blend shows a lower volume fraction than the Ca based oils at all temperatures starting with 300 °C. The volume fraction decreases to around 0.1 % and starts to stabilize at temperatures above 700 °C. The 101A (Zn/S/P) displays a much smaller volume fraction than the other blends even at 300 °C. The 300 °C volume fraction penetrating the oven was measured to be around 10^{-5}. The volume fraction was shown to stabilize after 700 °C for all the oil sprays and only decreased modestly between 700 and 1100 °C. 1100 °C was used as the standard test condition to insure that

a stable and complete metallic ash was sampled. Based on the chemical equilibrium models Ca and Mg should form the stable compounds CaO and MgO respectively at high temperatures. This appears to be fairly consistent with the ash volume fraction versus temperature trends.

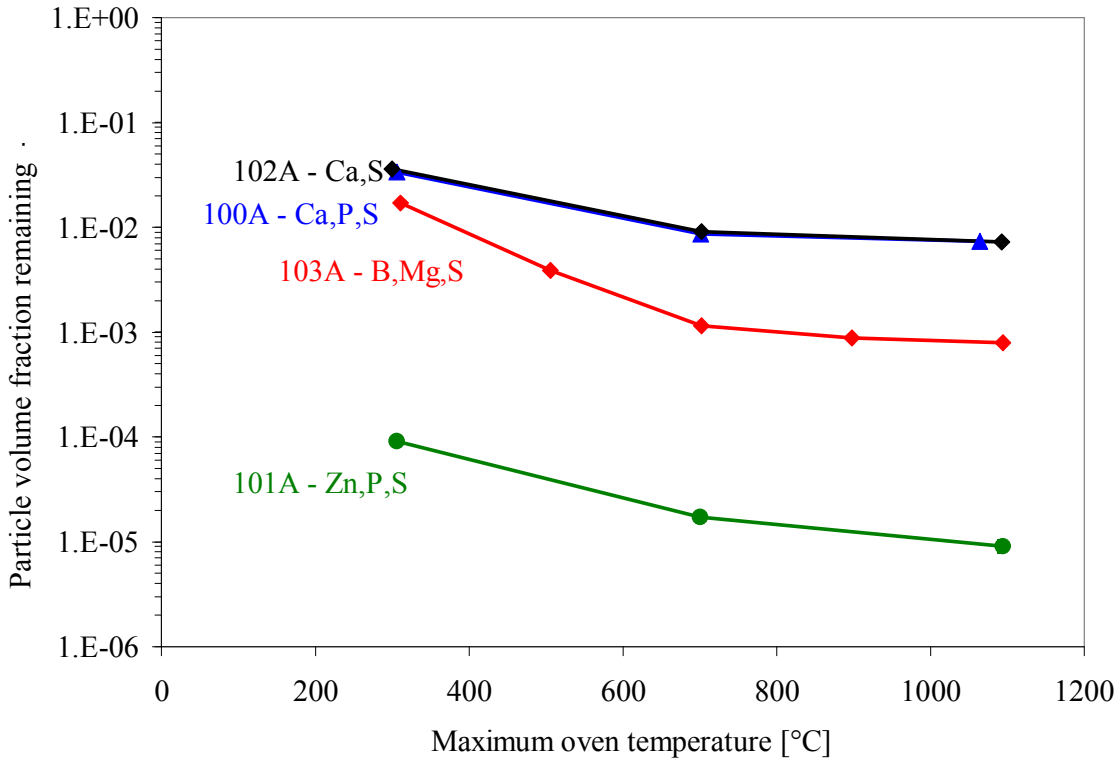

Figure 25: Particle volume fraction remaining after oven treatment plotted against maximum steady-state oven temperature

Table 10 displays the measured and expected ash particle volume fractions based on the elemental metallic content in each oil blend and the ratio of the measured fraction to the expected fraction. It was assumed that the ash consisted of the pure compounds as indicated. Based on this analysis, the ratios of measured-to-expected volume fractions were 2.1 and 2.5, 1.5, and 0.02 for the Ca blends, Mg blend, and Zn blend, respectively. The over prediction of ash fractions by the HTOM for Ca and Mg oil blends is at first somewhat disconcerting. The downstream oven concentrations were all corrected for thermophoretic losses and at 1100 °C the correction factor used was 0.56. This could

make up for the factor of 2 difference; however thermophoretic particle losses are real and need to be taken into account. Size distributions of the oil spray and ash particles in Figure 24 show that a significant portion of the oil spray volume distribution is likely located above the upper size limit of the SMPS while nearly all of the ash volume falls within the sizing range.

Table 10: Calculated expected metallic ash fractions based on metallic additive concentrations compared with measured values

				Metallic Volume Fraction		
Blend #	Element	Compound	Concentration [ppm]	Expected	Measured	Measured/Expected
100A	Ca	CaCO3	3946	2.9E-03	7.3E-03	2.51
101A	Zn	ZnSO4	1008	5.9E-04	9.6E-06	0.02
102A	Ca	CaSO4	3724	3.4E-03	7.2E-03	2.10
103A	Mg	MgCO3	500	5.3E-04	7.8E-04	1.48

Note: Expected concentrations are based on the assumption of spherical particles of the compound listed

As shown in Figure 26, a lognormal fit to a typical lube oil size distribution reveals that roughly half the volume concentration could be located above the sizing range of the SMPS configuration. When this is taken into account the Mg ash measurements move from 48 % over predicting to roughly 25 %.

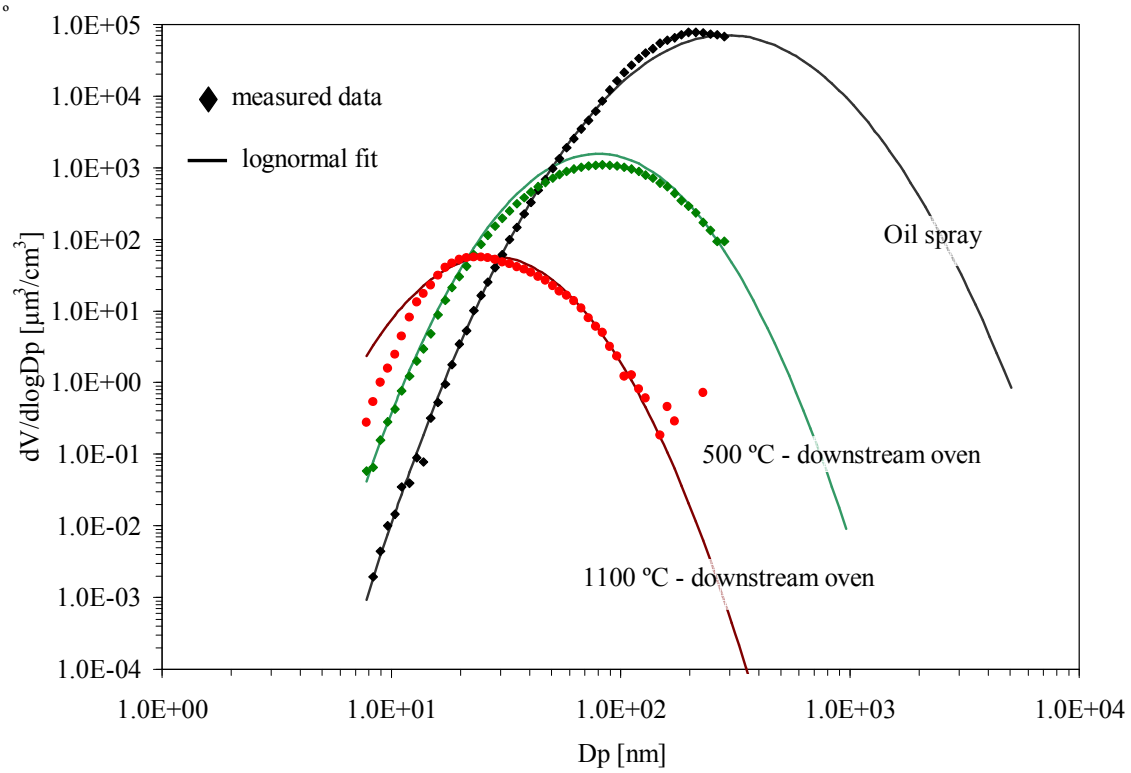

Figure 26: Lognormal curve fit of 103A (Mg/B) lube oil spray upstream and downstream oven volume weighted size distribution

The consistent over prediction of the Ca and Mg based oils creates some doubt in the measurement calibration. A logical hypothesis is that when the atomized oil size distribution is sampled the more volatile portion of the lube oil has been removed by the activated carbon. The removal of part of the lube oil leads to under measuring the lube oil spray volume concentration and to the over calculation of the ash system penetration ratio.

It is clear from Figure 25 that even at 300 °C the volume fraction of particles downstream of the oven with the Zn additive spray is more than 2 orders of magnitude lower than for the Ca and Mg additives. This is not fully understood. The Zn content of this additive is about 1000 ppm compared to about 4000 ppm for the Ca additives and 500 ppm for the Mg additive. Thus, it might be expected that the volume fraction downstream of the oven would fall between those of the Ca and Mg additives. Previous chemical equilibrium modeling indicates that the main Zn compound expected below

about 700 °C is solid ZnSO4. Above that temperature gaseous Zn is predicted. However, the chemical equilibrium dataset only contained a small number of Zn compounds and did not have the specific species of Zn contained in the lube oil. The Zn used in lube oil additives is usually a zinc dithiophosphate (ZDDP), which is meant to react with engine surfaces at fairly low temperatures (~100 °C) and form anti-wear coatings (Caines and Haycock 1996). Therefore, the Zn in the lube oil sprays might be removed at fairly low temperatures by decomposition of ZDDP to form gaseous species that deposit on the internal walls of the apparatus through diffusion. At first this would seem inconsistent with the significant Zn deposits of varying composition found in used DPFs such as $MgZn_2(PO_4)_2$ and ZnO reported by Sappok, et al., 2009 and $Ca_{19}Zn_2(PO_4)_{14}$ and $CaZn(PO_4)_2$ reported by Lambert, et al., (2010). However, it may be that gaseous Zn compounds diffuse to the walls of exhaust system components and subsequently react with other depositing materials. These results suggest that the mechanism of deposition metallic ash compounds on engine, exhaust system, and aftertreatment system depends on the detailed composition of the additive, with the Ca and Mg formulations used here forming ash likely to deposit mainly as particles and Zn formulation forming volatile compounds likely to deposit mainly as gases.

Chapter 4: Engine exhaust ash results and discussion

4.1 Engine exhaust ash determination

Figure 27 shows an example of engine exhaust particle volume fraction measured downstream of the tube oven at temperatures between 900 and 1150 ºC. The trend is a good representation of other data in that the volume fraction is reduced until around 1100 ºC. After which, it stays constant. The combustible fraction appears to be completely oxidized at 1100 ºC and can therefore be labeled as ash. Unless otherwise noted, all engine ash results were taken at an oven temperature of 1100 ºC.

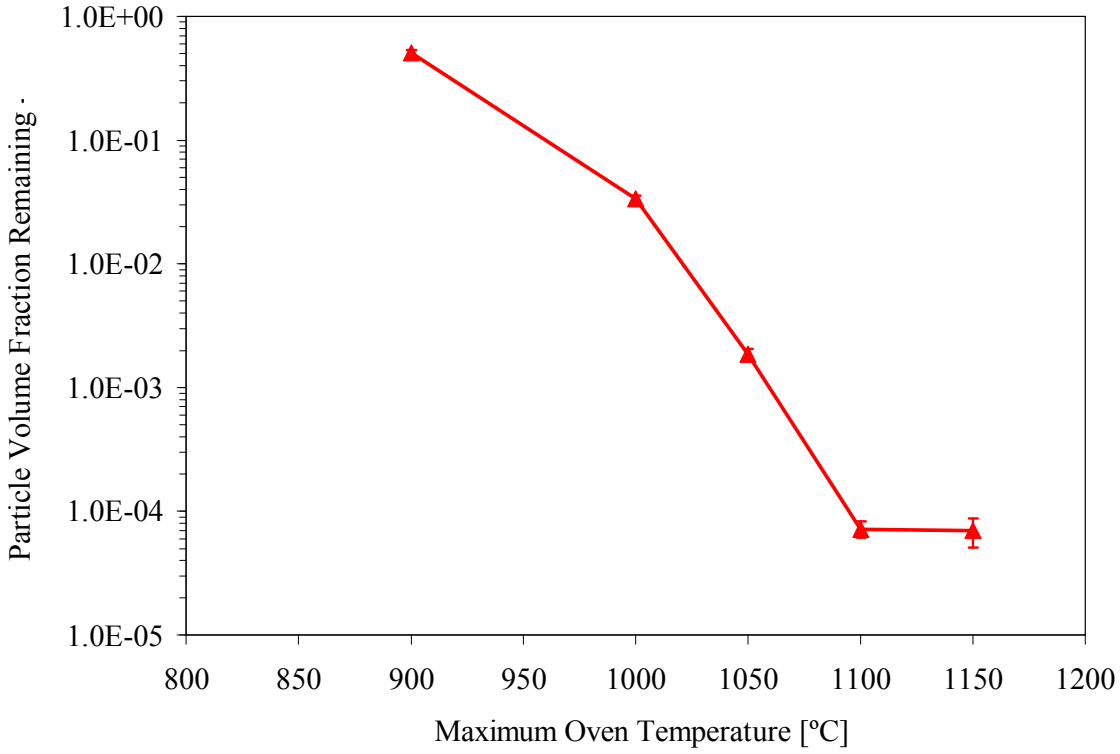

Figure 27: Engine exhaust particle volume fraction penetrating tube oven
(Note: exhaust measurements from a Cummins ComfortGuard APU at 0 % load)

4.2 Engine ash repeatability study

Figure 28 displays the results from engine exhaust sampling from the VW TDI engine at a constant speed and engine load before all the apparatus upgrades were completed. Shown are the total exhaust particle volume concentrations, ash particle volume concentrations, and the ash volume fractions. The ash particles were measured

after passing through a high temperature tube oven with a set point of 1100 °C. It should be noted that different fuels were used as noted on the figure; including BP-50 (50 ppm S), ECD-1 (<10 ppm S), and BP-6 (6 ppm S). For the most part the total particle volume concentrations were similar. The ash particle volume concentrations varied by more than two orders of magnitude in some instances. The magnitude of the differences seen in ash emissions suggests that the apparatus variability could be affecting repeatability along with possible variations in the actual emissions.

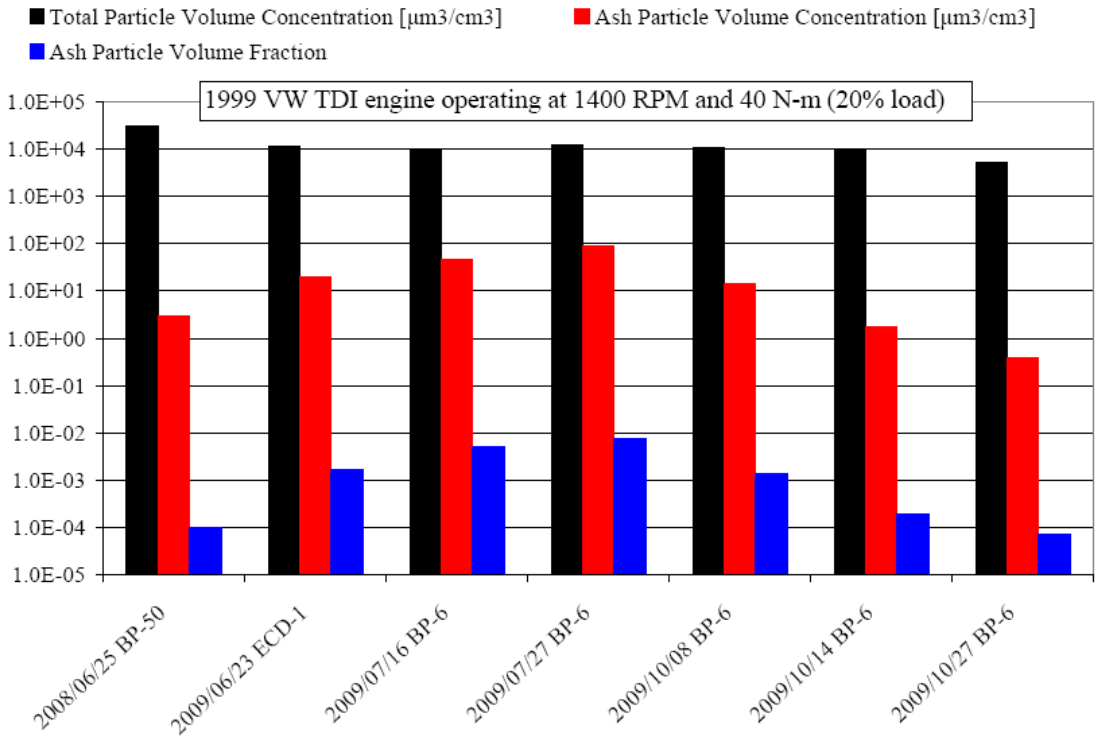

Figure 28: Total particle and ash volume concentrations along with the ash volume fraction from several tests

The first four data sets shown in Figure 29 show the volume concentrations and ash fractions measured after all the upgrades were made to the HTOM. They are repeats of the test conditions shown in Figure 28. The total particle volume concentrations were slightly less than what was seen before, and the ash volume fractions are more repeatable than previously seen. Because of the improved repeatability shown in the lube oil spray

experiments, it was determined that the variation in ash emissions is most likely attributable to real aerosol variation and not measurement variability. Ash volume fractions were about 1 x 10^{-4} for the four tests. The last two data sets displayed in Figure 29 show the results of tests made two days apart with the Cummins generator operating at 3600 rpm with no external load. The total exhaust volume concentrations were very similar and the ash concentrations showed some differences of the same magnitude seen in the most recent VW TDI exhaust measurements.

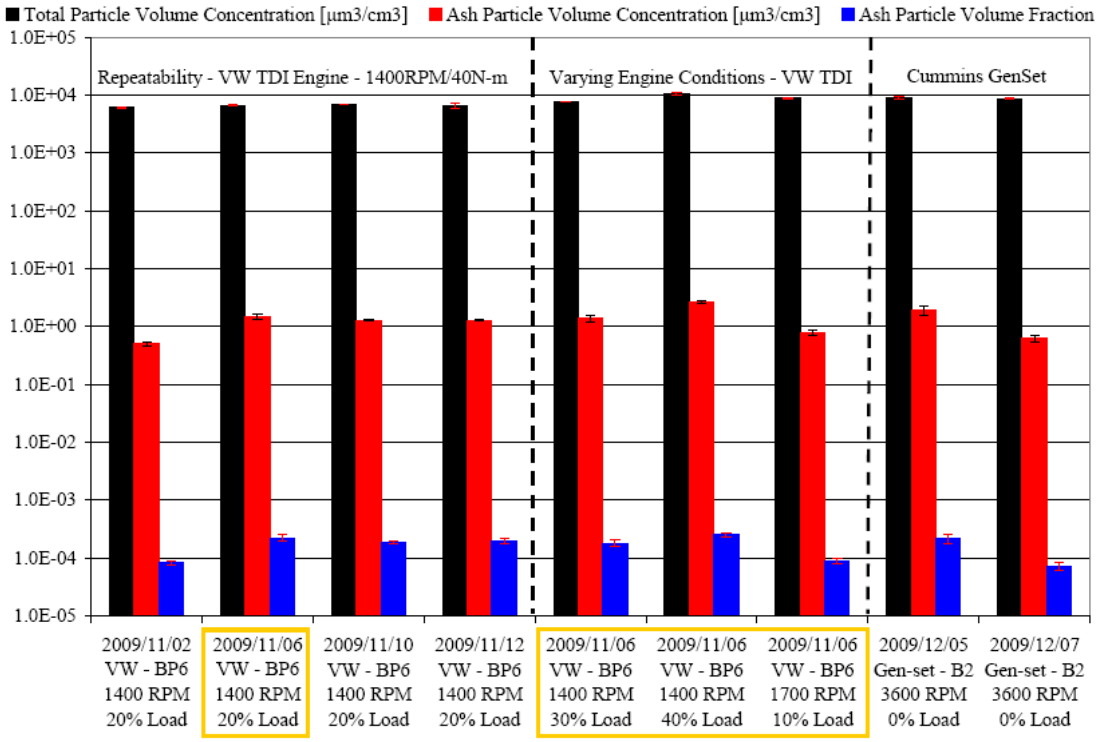

Figure 29: Total particle volume concentrations, ash volume concentrations, and ash volume fraction of engine exhaust sampled from VW and Cummins APU engines (Note: Orange boxes indicate results from the same day and the error bars represent one standard deviation taken from the average of at least three samples)

Figure 30 shows total particle and ash volume weighted size distributions. The total exhaust distributions are similar except for small discrepancies for particles < 20 nm. Between 30 and 80 nm the ash particle size distributions lie very close to one another. The 11/2/2009 ash distribution shows significantly lower volume concentrations

below 20 nm compared to the other two tests. There were also variations in the ash size distributions above 80 nm most likely due to poor counting statistics. With the improved system, it is believe that these day to day variations are due mainly differences in engine ash emissions. The shape of the ash distributions suggests that there are particles present above the sizing range used for the SMPS in these experiments.

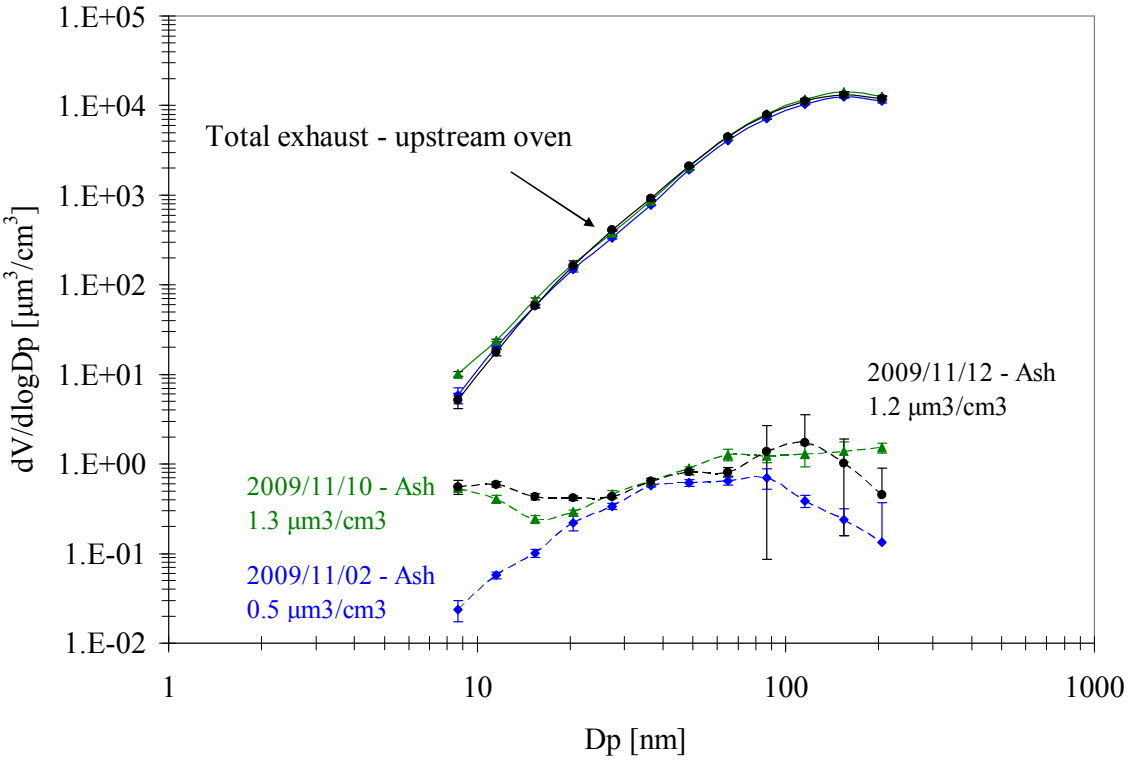

Figure 30: Selected averaged volume weighted size distributions of VW TDI engine out and downstream oven (1100°C) or ash samples from updated HTOM apparatus (Note: 1999 VW TDI engine at 1400 RPM and 40 N-m (20% load); error bars represent one standard deviation of the average of at least three samples; corrected for dilution and post-oven thermophoretic losses)

4.3 Steady-state engine exhaust ash

The HTOM was used to make steady-state engine ash emission measurements for different engines and engine conditions. Figure 31 shows volume weighted size distributions of samples collected from the Cummins APU exhaust. These data represent averages taken from two different test days, and on the second day three load conditions

were tested. The 0 % load total particle distributions from the two days are very repeatable, suggesting a stable engine. As load was increased, total particle volume concentrations increased. The increasing load led to a decrease in particles smaller than 30 nm and an increase in concentrations of particles larger than 70 nm. This trend is similar to the particle number to volume ratio trends discussed in the literature (Kittelson 1998; Liu et al., 2003). The three ash distributions from 12/7 show an increasing trend in ash particles for most sizes as load increases but unlike the soot particles the volume weighted diameter is smaller at the highest load than at the lighter loads. The two 0 % load ash distributions are similar for particles less than 20 nm and deviate at sizes larger than 20 nm.

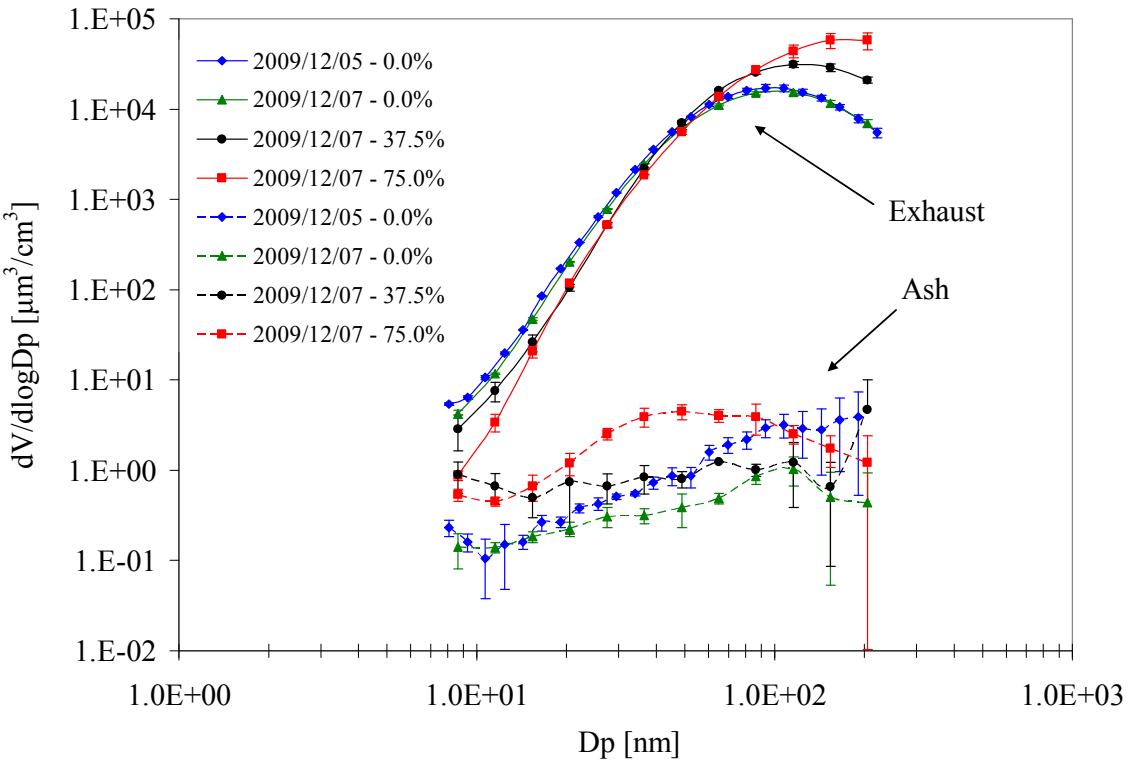

Figure 31: Averaged volume weighted size distributions of Cummins APU up and downstream oven (1100°C) from updated apparatus
(Note: Cummins APU exhaust; corrected for dilution and thermophoretic losses; error bars represent one standard deviation from at least three samples taken at each condition; % refers to percent of peak engine load)

The majority of the particle number is found in particles smaller than 20 nm while the larger particles that account for most of volume have very small number concentrations, near the limits of detection, thus increasing variability. Except for the highest load, the ash size distributions appear to be truncated with considerable volume above the upper sizing limit of the SMPS. There was some evidence of this in the VW results, but the trend is stronger with the Cummins APU.

Figure 32 displays the ash volume fractions plotted against engine load for both the VW and Cummins APU tests. The APU data show a near linear increase in ash volume fraction with engine load, which is consistent with earlier work (Apple, et al., 2009). The VW data cover a much smaller range of engine loads, and the trend of the ash fraction increasing with load is not as apparent as a result of larger run to run variability. These variations appear to be real and are most likely not due to measurement error. A measurement made with the VW operating at 1700 RPM is also plotted and is very close to the 1400 RPM results at the same load.

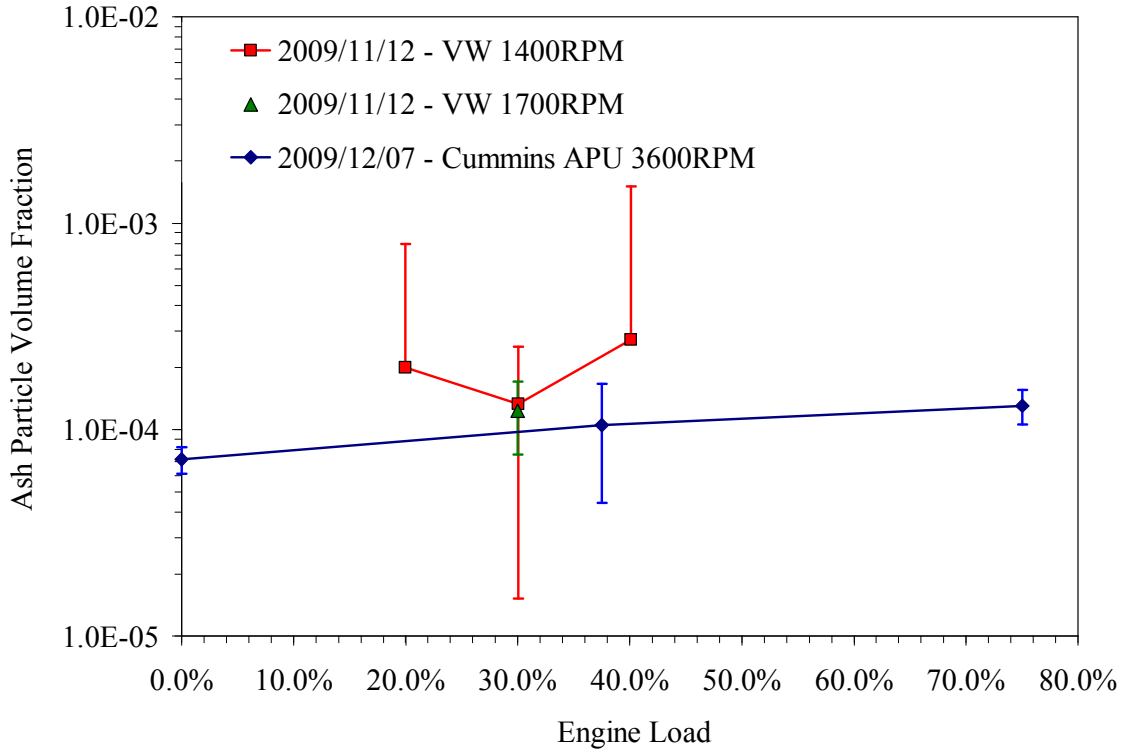

Figure 32: Ash volume fraction versus load for constant engine speeds from engine exhaust ash experimentation (Note: Error bars represent one standard deviation from at least three samples taken at each condition)

Figure 33 shows the calculated oil consumption against engine load for the Cummins APU. The trend is not quite linear, but there is a slight positive correlation between oil consumption and steady-state load. The specific lube oil consumption rates were calculated as 0.025 and 0.021 g/kW-h for the 37.5 and 75 % load conditions. The measured oil consumption rates are less than expected based previously cited rates.

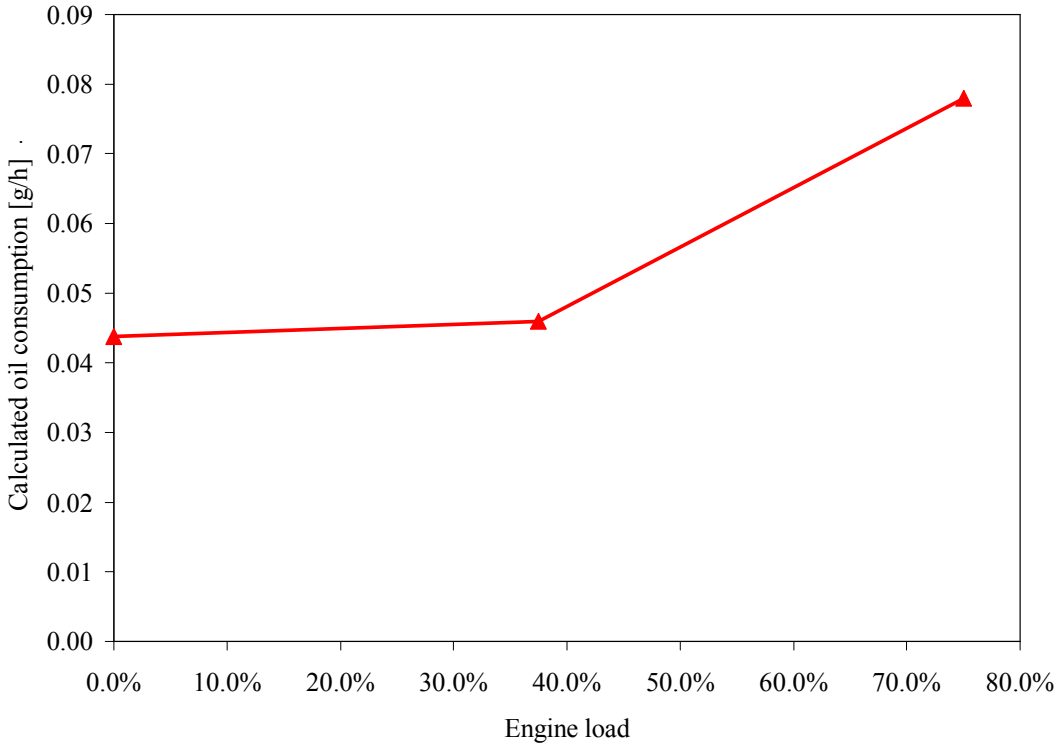

Figure 33: Oil consumption calculated from measured ash emissions for different engine loads (Cummins APU)

4.4 Lube doped fuel exhaust ash

Ash emissions were studied further by doping Diesel fuel with lube oil. This effectively increased the lube oil consumption of the engine by a known amount. The Ca containing lube oil blends were selected for these tests. This was because the lube oils were of known ash composition and contained ash to which the HTOM was particularly sensitive.

Using the known Ca concentrations in the 100A blend and the known fuel doping rate of 1.0 % the expected ash emissions were calculated. Ca was assumed to be in the form of $CaSO_4$ while in the lube oil and CaO downstream of the oven. A mass balance was then performed to calculate the ash penetration through the engine and tube oven. Figure 34 shows the results for the ash penetration at different oven temperatures. It was expected that the penetration was not 100 % due to measurement losses along with losses

inside the engine. At 1100 ºC the 100A result appears less than previous work. Kim (2005) reported ash penetrations of more than 50 %.

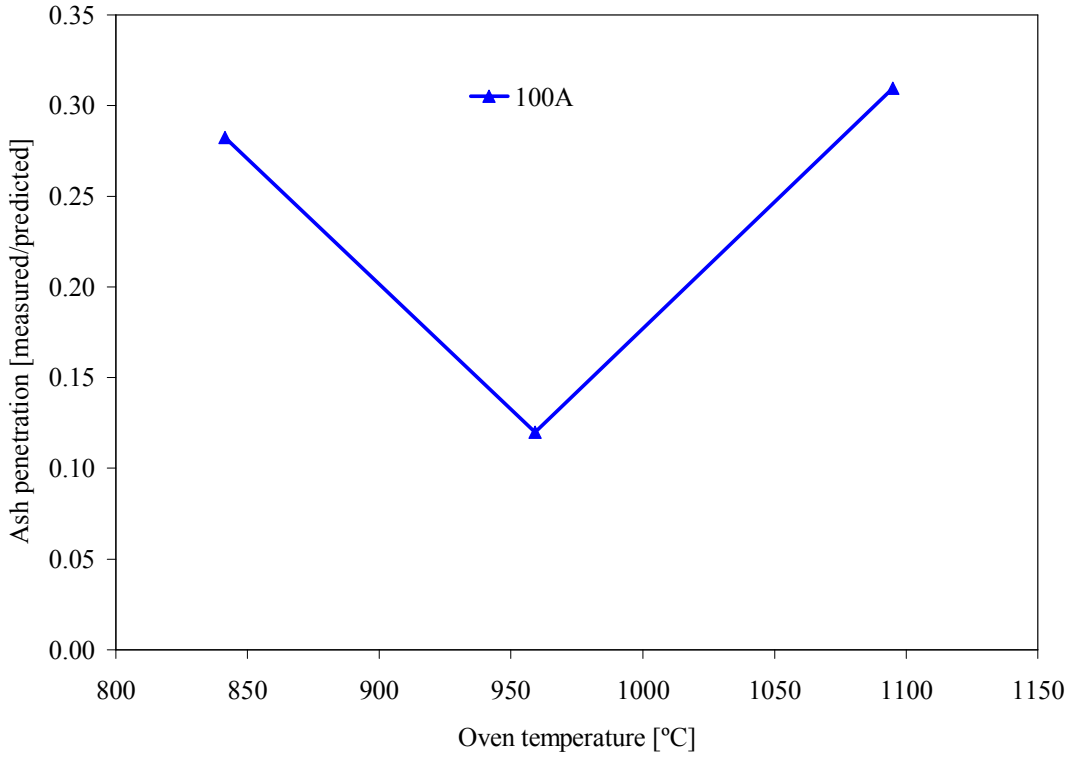

Figure 34: Exhaust ash penetration from lube oil doped fuel to HTOM ash measurement (Note: Cummins ComfortGuard APU at 0 % load; ULSD fuel doped with 1 % 100A lube oil blend)

The trend in Figure 34 where the ash penetration decreases up to 950 °C followed by an increase was not fully understood. For a constant engine speed and load the ash penetration would be expected to stabilize or decrease with an increasing temperature. This test was repeated twice by ramping oven temperatures in both a positive and negative direction with similar results. More experimentation is needed to understand this phenomenon.

4.5 Transient engine ash emissions results

The ability of the HTOM to make real-time ash measurements was demonstrated on the VW engine. An EAD was used for making ash particle measurements. The EAD

measured the real-time particle diameter concentration. The diameter concentration is defined as the length of a chain with all particles from 1 cm^3 (TSI Incorporated, 2004). Diameter concentration (d^1) is closer to the desired volume (d^3) concentration measurement than a stand-alone CPC which measures number (d^0) concentration. Figure 35 shows a strip chart of ash particle length concentration measured downstream of the oven during two engine load steps. Prior to the first reduction in load, the engine was allowed to stabilize at 80 N-m. At the first load transition, a large spike occurs in ash concentration almost 4 times the previous steady-state concentration. After the reduction in load the engine stabilized and the ash emission stabilized at a lower concentration. The load was then increased to 100 N-m which featured an even larger spike in ash particle concentration. The ash emissions then reduced to a steady state level as the engine stabilized.

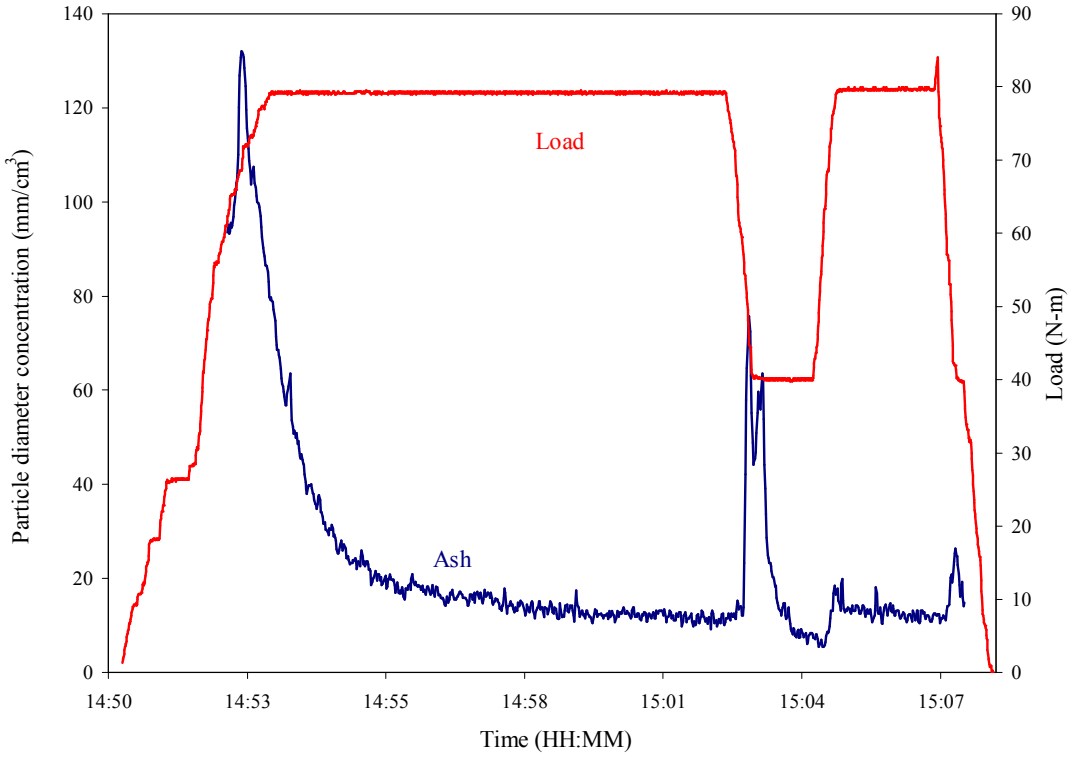

Figure 35: Real-time ash particle length concentration strip chart for two major engine load steps at a constant speed
(Note: 1.9 L VW TDI engine at 1400 RPM with < 15 ppm Diesel fuel)

Prior to the initial load step the engine was warmed up at idle. Lube oil build-up on the cylinder wall during this period could have been the cause for the large spike in ash emissions during the first load increase during which the excess oil would have been consumed. Overall, the transient spikes in ash emissions are expected. Froelund et al. (2001) shows repeatable oil consumption spikes during transient engine cycles.

4.6 Ash penetration of loading DPF

Downstream DPF number and volume concentrations of particle samples taken at various times from the start of the filter loading are shown inTable 11. The results shown include the raw exhaust number concentration and the downstream oven number and volume concentrations corrected for dilution and thermophoretic losses. Since the EEPS is a real-time instrument the EEPS concentrations are 60 s averages while the SMPS concentrations are derived from one 60 s scan. The raw or uncorrected downstream DPF exhaust particle concentrations ranged from a few thousand to a few hundred particles per cubic centimeter. After making the correction for dilution, the particle concentration downstream of the DPF was 4.8×10^5 at 3 min in to test 1 and 2.6×10^6 part/cm^3 at 5 min into test 2. After about 30 min of loading the concentration ranged between 1 to 5×10^5 part/cm^3 for the two tests. Both number and volume concentrations decreased around two orders of magnitude over the course of both tests.

Table 11: Total raw and corrected particle concentrations measured by the SMPS and EEPS downstream the filter during filter loading experiments

				Raw	Corrected*	
Test	Aerosol	Instrument	Time	#/cm^3	#/cm^3	um^3/cm^3
1	Total Exhaust	SMPS	0:03	3.2E+03	4.8E+05	5.2E+02
1	Total Exhaust	SMPS	0:12	5.1E+03	7.6E+05	2.9E+02
1	Total Exhaust	SMPS	0:34	4.4E+02	1.1E+05	1.6E+01
1	Ash	SMPS	0:03	2.2E+03	1.6E+04	3.0E-02
1	Ash	SMPS	0:23	9.4E+01	6.8E+02	1.1E-02
1	Ash	SMPS	0:35	6.0E+00	4.3E+01	1.3E-02
2	Total Exhaust	EEPS	0:05	3.28E+04	2.6E+06	1.5E+03
2	Total Exhaust	EEPS	0:21	3.89E+03	3.1E+05	1.4E+02
2	Total Exhaust	EEPS	0:28	1.31E+03	1.0E+05	4.8E+01
2	Ash	SMPS	0:06	1.9E+04	2.3E+05	1.3E+00
2	Ash	SMPS	0:22	1.5E+03	1.8E+04	2.1E-02
2	Ash	SMPS	0:38	3.1E+01	3.8E+02	1.1E-02

*Corrections were made for dilution and thermophoretic loss downstream oven

Table 11 also shows volume concentrations of ash particles downstream of the oven during the loading of the DPF. The raw number, corrected number, and corrected volume concentrations are shown. After more than 20 min of filter loading the measured ash concentration was < 100 part/cm^3, which is very low even for the SMPS. It should be noted it is often difficult to measure concentrations downstream of a DPF. Here, exhaust ash concentration were measured at 3-4 orders of magnitude lower. Errors caused by the low concentrations are magnified by corrections made for dilution and thermophoretic loss after the oven.

Figure 36 shows the particle volume concentrations versus time for the loading of a DPF on two separate days of testing corrected for dilution and thermophoretic losses. The time scale was measured from the beginning of each day's test. The black and gray lines show particle concentrations measured downstream of the DPF from the two tests. The total DPF particle emissions appear to decrease exponentially for both tests as the filtration efficiency of the DPF increases as it is loaded with exhaust material. The volume concentration trends agree fairly well between test 1 and 2. The EEPS concentrations are slightly higher than the SMPS. Actual differences in DPF behavior from test to test could have caused the discrepancies. The EEPS has a higher lower

detection limit than the SMPS and it becomes less reliable as concentrations approach 1,000 part/cm^3 so that an increasing amount of scatter appears towards the end of the test due to low particle number concentrations.

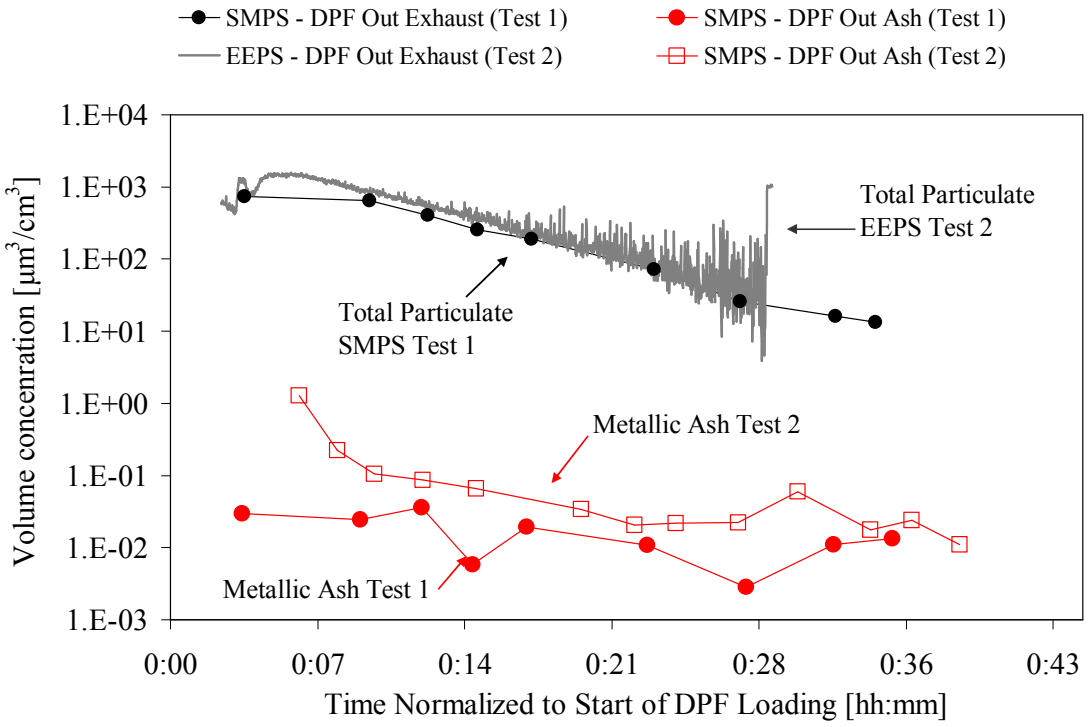

Figure 36: Total particle and ash volume concentrations measured during filter loading (Note: Corrected for dilution and thermophoretic losses)

Total particle volume weighted size distributions obtained from the EEPS and SMPS data are shown in Figure 37. The SMPS size distributions from test 1 show a decrease in magnitude for the size bins between 70 and 200 nm throughout the test. The size distribution at 34 min obtained from test 1 has several size bins that were recorded as zero particles. This was most likely due to the distribution statistics created by very low particle concentrations near the lower limits of detection. The size distribution at 12 min showed more particles below 50 nm than the other two distributions but this still accounted for a tiny fraction of the volume. The size distributions from the EEPS from test 2 show a considerable decrease in magnitude with time between 70 and 200 nm, and

irregularities appear in the size distribution for particles > 300 nm, but these tails correspond to little volume and are likely associated idiosyncrasies of the EEPS inversion software.

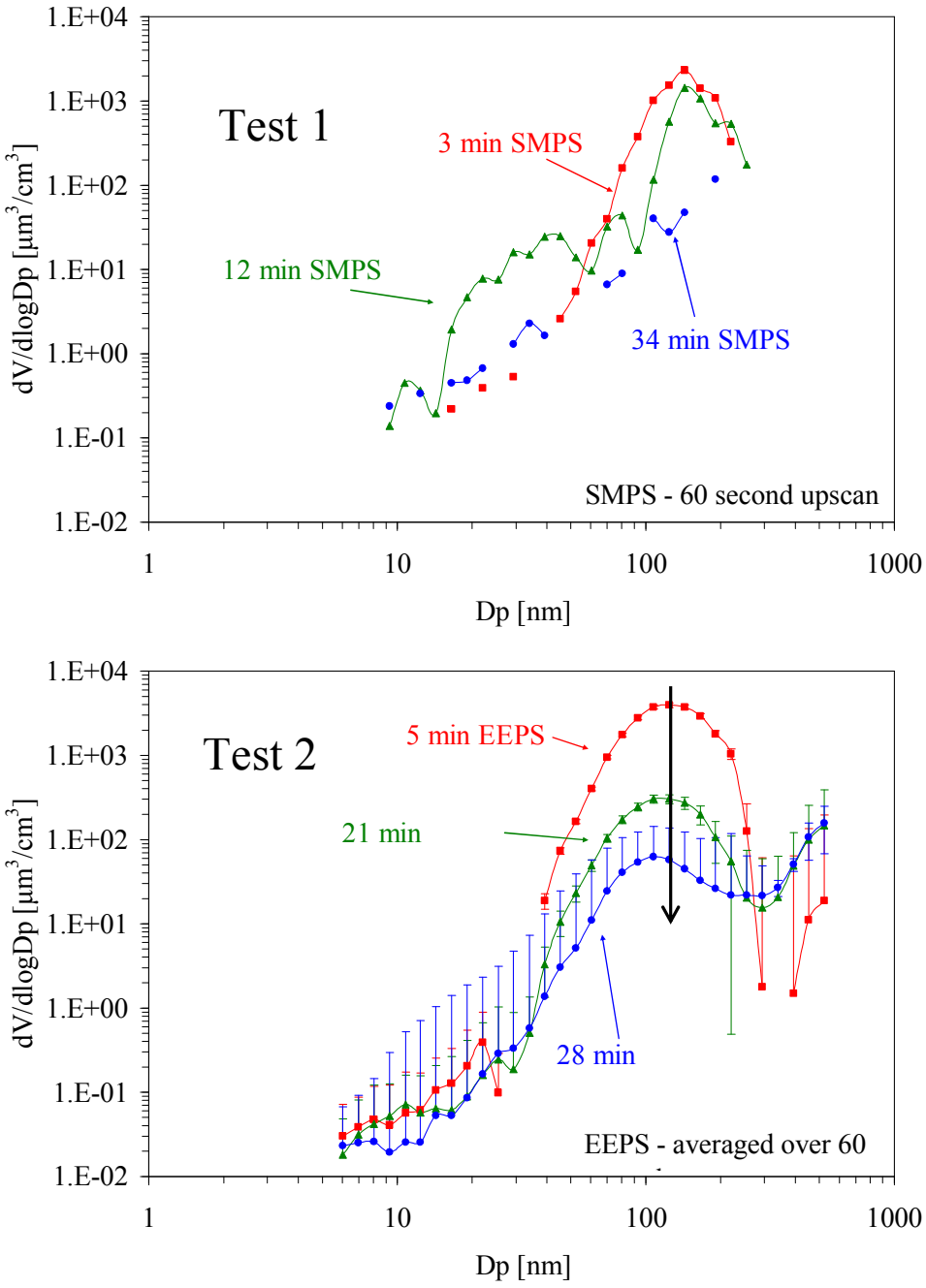

Figure 37: Volume weighted size distribution of particles measured downstream of the DPF during loading
(Note: VW TDI engine exhaust at 1400 RPM and 40 N-m load, EEPS (Test 2) distributions are averaged over 60 s and SMPS (Test 1) distribution is from a 60 s scan)

Figure 36 also shows the trends in ash emissions from the DPF during loading. The initial ash concentration is quite different between the two tests, the initial volume concentrations of ash particles are over an order of magnitude different. After a loading period of about 10 min the concentrations converge slightly. Test 1 shows a small decrease in ash emissions between the first and last data point while test 2 shows a much larger decrease between the first and last scan which is in better agreement with the two orders of magnitude reduction seen in the total exhaust concentrations. The ash concentrations varied significantly with time in both tests, especially in test 1 where ash concentrations were very low and near the limits of detection. The low concentrations lead to irregularities in the size distributions from size channels sporadically showing zero counts. These zeros are due to the SMPS scanning the size range over the course of 60 s. At low concentrations few particles are counted in each size channel and due to normal counting statistics some channels may have zero counts. Longer scan times improve counting statistics but reduce the time resolution of the size distribution measurements. This can be seen in Figure 38, which shows selected ash particle distributions during the DPF loading tests. The distributions are volume weighted and do show a decrease in magnitude over time. However, the irregular zero counts could influence total concentration measurements since they are calculated by integrating the size distribution data. Methods to mitigate these problems include lengthening SMPS scan times, and using fewer and larger particle size bins. Another problem could be that some of the ash particles are not counted because they are outside of the sizing range of the instruments.

Previous work has shown that ash can be evenly distributed on soot particles (Miller et al. 2007). If the ash reduction does not track the soot particle reduction it is either due to a non-uniform distribution of ash amongst the soot or a change in the composition of the aerosol penetrating the DPF. Chemical equilibrium calculations indicate that ash constituents like Ca and Mg compounds undergo gas to particle formation during the expansion stroke after soot formation has taken place and thus might be expected to deposit on the surface of the soot particles. This is consistent with the observations of Miller, et al. showing ash particles decorating the surface of soot

particles. If most of the ash is present on the surface of the soot the ash volume would be expected to track with soot surface area rather than volume. In Figure 39 the measured soot surface areas are compared with ash volume concentrations. Although there are some deviations, the ash volume tracks soot surface area better than the soot volume that was shown in Figure 36.

Other issues are likely to influence the ash associated with particles downstream of a DPF. Run to run differences in regeneration may have an influence, especially in initial ash emissions. There also may be storage and release effects and other issues that are not fully understood because tests of this type have never been done before. In any case, although there was significant scatter in the results, these tests demonstrate that real time ash measurements downstream of a DPF are possible using the HTOM.

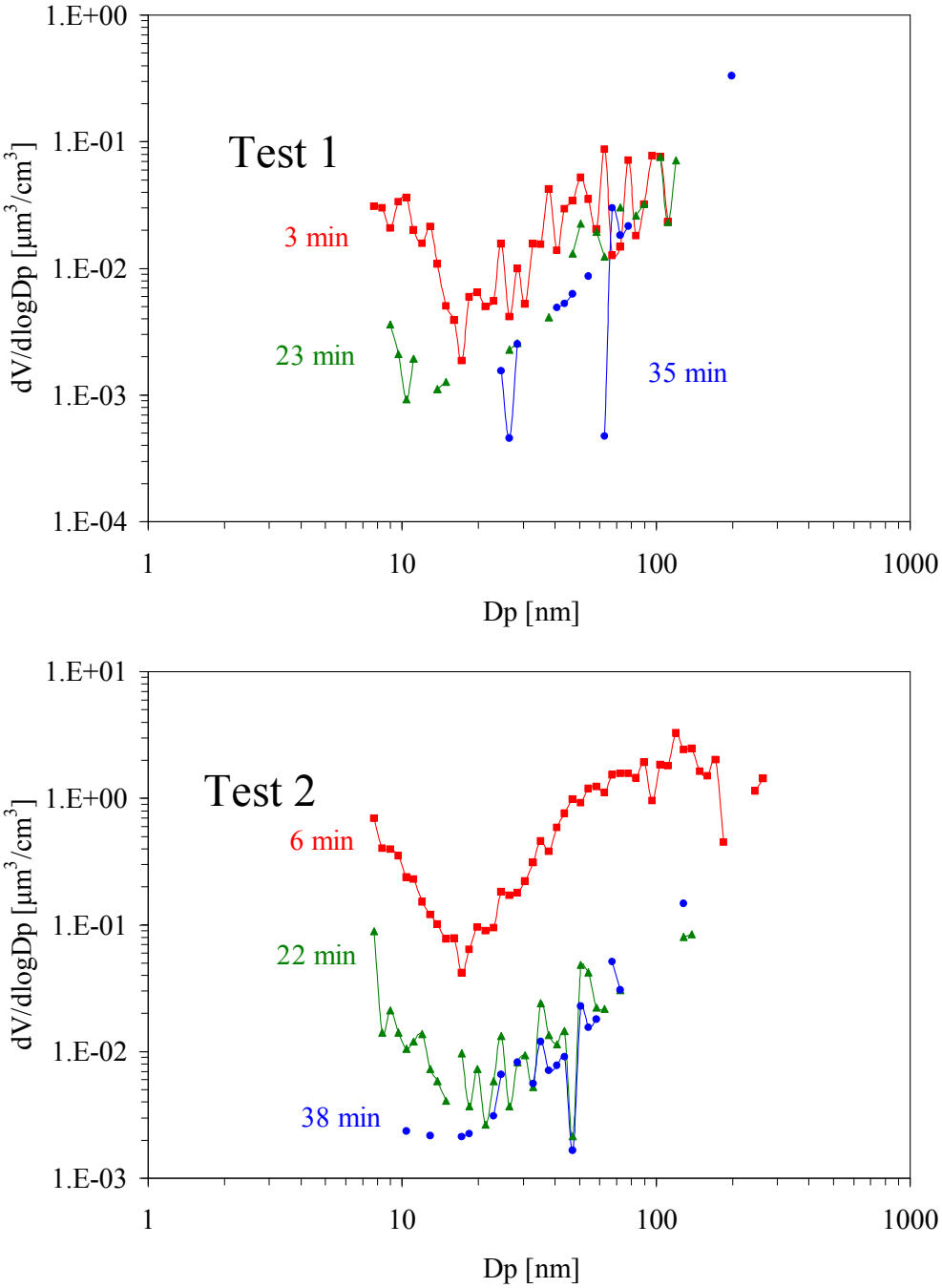

Figure 38: Ash particle volume weighted size distributions measured downstream of the DPF during loading, from SMPS using 60 s scans
(Note: VW TDI engine at 1400 RPM and 40 N-m load; ash particles from tests 1 and 2 after 1100 °C oven)

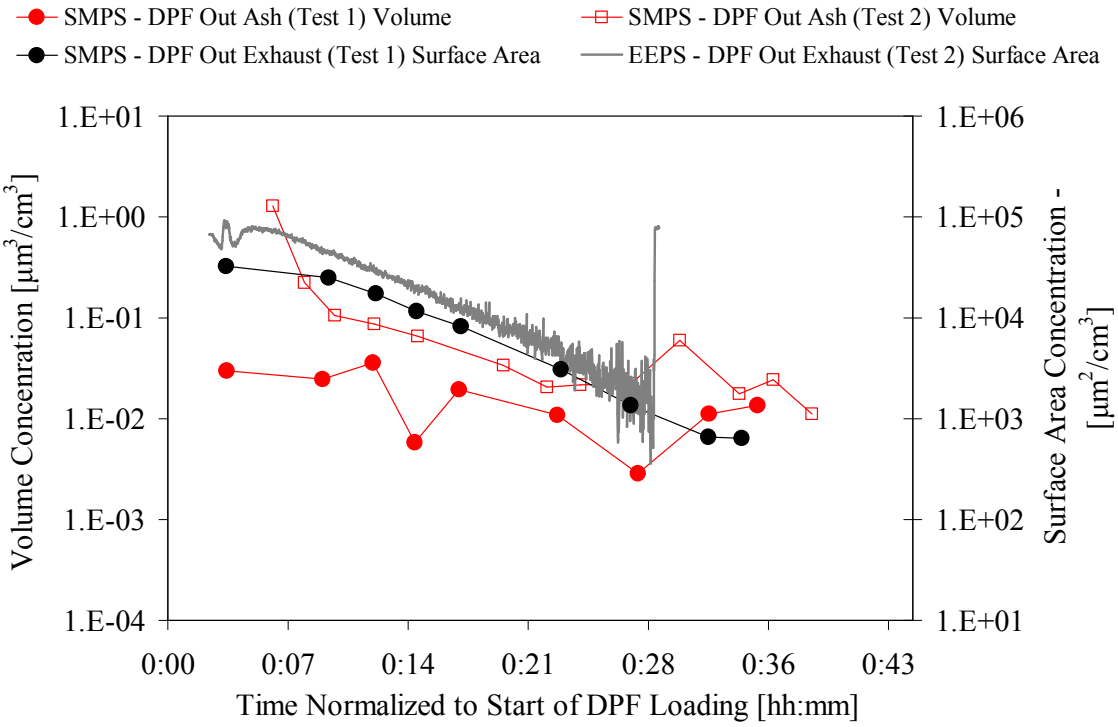

Figure 39: Total soot particle surface area and ash volume concentrations measured during DPF loading

Chapter 5: Conclusions and recommendations

5.1 Conclusions

The first goal of improving the HTOM apparatus and methodology was completed. Particle losses were minimized by removing some unnecessary system components such as a coiled cooling section downstream of the oven. Particle oxidation was improved by increasing particle residence time inside the heated length of the oven. The signal-to-noise issues were improved by reducing sample dilution. However, low ash concentrations still cause measurement challenges.

Measurement repeatability was improved. This was achieved by finalizing all improvements and stabilizing the oven temperature profile. Figure 40 shows a plot of repeated lube oil spray and engine exhaust ash volume fraction measurements. Focusing on the VW exhaust data, it can be seen that the ash volume fraction increased significantly leading up to the fuel pump rebuild and re-setting of the injection timing. This could have been caused by the leaking fuel pump.

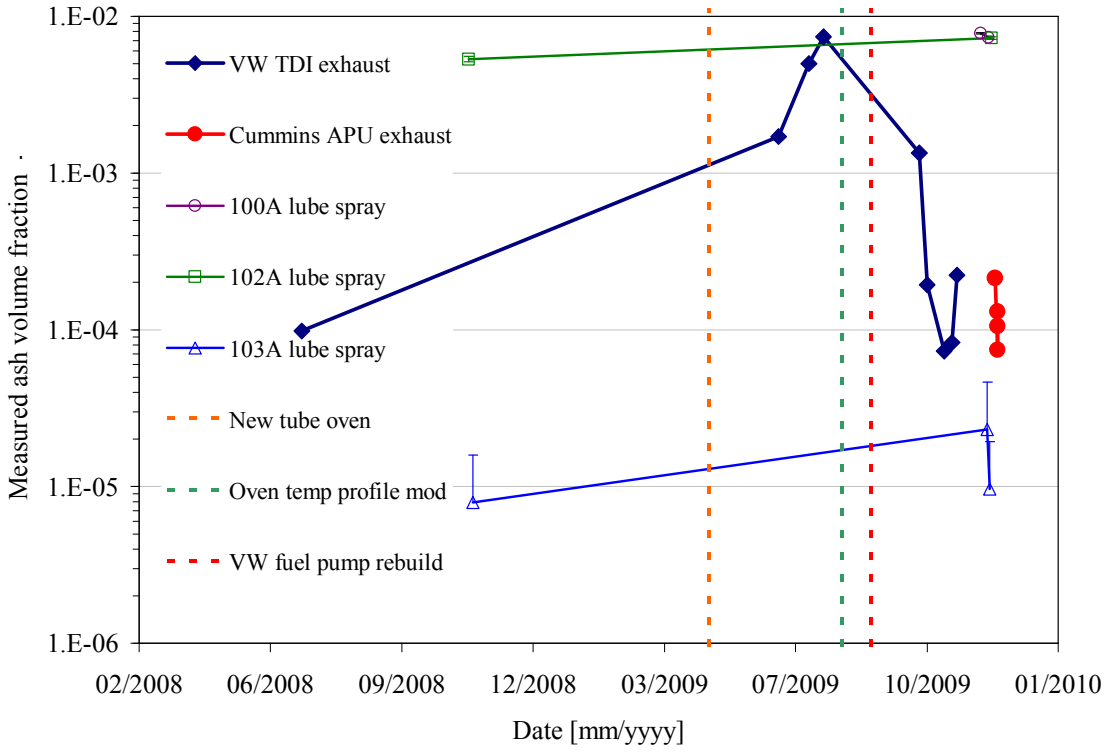

Figure 40: Measured ash volume fractions for lube oil sprays and engine exhaust throughout the project highlighting improved repeatability and major apparatus events

The lube oil spray proved to be very useful for validation of the HTOM repeatability. Due to the varying nature of experiments and modifications to the apparatus, initial lube spray and engine exhaust ash repeatability was an issue. After final system modifications were made, the lube oil spray experiments showed a significant increase in repeatability. Because of these results, any differences in repeated engine exhaust ash measurements greater than 10 % could most likely be attributed to variations in the actual exhaust and not the instrument. Even so, repeatability calibration with atomized lube oil should be carried out frequently. Analysis of engine exhaust data showed an improvement in repeatability. Based on the lube oil spray repeatability, test-to-test variations in exhaust ash measurements could be mostly attributed in variations of actual engine ash emissions.

The HTOM proved to be sensitive to Ca and Mg based ash species. This was confirmed by basic chemical equilibrium modeling where stable oxides were formed at high oven temperatures. The Zn based lube oil did not give expected results. The HTOM signal from Zn was not distinguishable from the base stock with no metallic additives. The chemical equilibrium model formulated for Zn species reveals that Zn tends to not oxidize easily and is at equilibrium as a gaseous Zn species at the upper oven temperatures. Zn based ash particles would not be expected if this gas either formed extremely small particles that diffused to the walls or was lost to the walls directly.

The analysis of expected ash compared to measured ash revealed that, as expected, the Zn based lube oil ash was under measured by the HTOM. However, the HTOM measured more than expected ash for the Ca and Mg containing oil sprays. The measured ash from the Ca oil sprays was 2.1 to 2.5 times the expected amount while the Mg oil spray was measured to have 1.5 times the expected ash. The used and fresh oil spray comparison also showed the HTOM over predicting the ash fraction. This could be the result of two factors. The apparatus and ash fraction measurement may be the culprit. The carbon scrubber that is used to remove the volatile butanol vapors before measuring the oil aerosol could also be removing a portion of the volatile fraction of the lube oil. This would effectively increase the metallic ash concentrations. The other factor is likely

the particle measurement range. Particle volume distributions show that a significant portion of the volume concentration is located above the upper limit for the SMPS configuration, further compounding over estimation of the ash fraction. Lognormal curve fits supported this concept. Overall, the lube oil spray showed that the HTOM is a repeatable but currently has some problems with accuracy.

Steady-state exhaust ash was measured along with exhaust ash from an engine with lube oil doped fuel. Oil consumption levels measured from baseline exhaust ash measurements were shown to be less than published values. Lube oil doped fuel measurements showed ash penetration from fuel to HTOM measurement to be 30 %. This is comparable but somewhat lower to previous work with this method. Ash measurements were also taken downstream of loading DPF. These measurements proved to be difficult due to very low particle concentrations. However, it was found that ash volume concentrations downstream of the DPF tracked better with soot surface area than volume concentrations which agrees with the idea that metallic ash 'decorates' the surface of Diesel soot particles after formation. More transient exhaust ash measurements were made to further demonstrate the HTOM's real-time capability. Engine out ash emissions were monitored in terms of ash particle diameter concentrations over several engine load steps. At the load steps spikes in ash emissions were seen.

5.2 Recommendations

Even though improvements were shown in the HTOM apparatus and methodology, there are still issues that need to be addressed.

- The over prediction of ash from lube oil sprays can be addressed by analyzing the lube oil spray between carbon scrubber and tube oven for ash concentrations. This will ensure that the problem lies with the activated carbon removing not only the butanol but a fraction of the oil.
- Thermogravimetric analysis on the Zn containing lube oil blend could be useful for studying Zn-compound survival at varying temperatures.
- Further characterization of engine out ash sensitivity should be examined as the baseline steady-state engine ash emissions were lower than expected even though

the survival of lube doped fuel ash was shown to be at 30 %.

- Further analysis could be completed on the morphology and composition of ash particles downstream of the oven using TEM and EDS.
- The implementation of a true real-time particle instrument should be made to fully take advantage of the real-time capabilities of the HTOM. This was done using the TSI EAD to some extent. Real-time measurements should be made with particle instruments that more closely quantify volume or mass concentrations. The EEPS could be used for these measurements. However, there is some concern with the signal-to-noise ratio of the EEPS. Another possibility is making real-time measurements using the SMPS in a single channel mode. The classifier could be set to a previously measured peak size in the ash distribution. The CPC would then be used to monitor the magnitude of the peak in real-time. The CPC number concentrations could then be fit to a curve to approximate a size distribution.

Bibliography

Abdul-Khalek, I. "Online Measurement of Volatile and Solid Exhaust Particles using a Catalytic Stripper System : Characterization and Application." M.S. University of Minnesota, 1996. Minneapolis, MN: .

Andrews, Gi E., et al. "The Measurement of Lubricating Oil Combustion Efficiency using Diesel Particulate Analysis." *Society of Automotive Technical Paper Series* (1998)

Apple, James, et al. "Measuring Diesel Ash Emissions and Estimating Lube Oil Consumption using a High Temperature Oxidation Method." *SAE international journal of fuels and lubricants* 2.1 (2009): 850-9.

Ariga, Susumu, Ping C. Sui, and Syed M. Shahed. "Instantaneous Unburned Oil Consumption Measurement in a Diesel Engine using SO2 Tracer Technique." *SAE International Journal of Fuels and Lubricants* (1992).

Baron, Paul A., and Klaus Willeke. *Aerosol Measurement Principles, Techniques, and Applications*. 2nd ed. New York: Wiley, 2001.

Bartley, G., and M. Khair. *Diesel Aftertreatment Sensitivity to lubricants/non-Thermal Catalyst Deactivation Consortium; Diesel Particulate Filter Study Summary Report*. SwRI® 03.05436 Vol. Southwest Research Institute, 2004.

Bodek, K., and V. Wong. "The Effects of Sulfated Ash, Phosphorus and Sulfur on Diesel Aftertreatment Systems – a Review." *SAE International Journal of Fuels and Lubricants* (2007): 2017.

Caines, A. J., and R. F. Haycock. *Automotive Lubricants Reference Book*. Warrendale, Penn: Society of Automotive Engineers, 1996.

Davies, C. *Aerosol Science*., 1966.

De Petris, C., V. Giglio, and G. Police. "Some Insights on Mechanisms of Oilconsumption." *SAE International Spring Fuels and Lubricants Meeting and Exposition* (1996)

Derjaguin, B. V., et al. "Measurement of the Coefficient of Thermal Slip of Gases and the Thermophoresis Velocity of Large-Size Aerosol Particles." *Progress in Surface Science* 43.1 (1993): 321-31.

Filice, M., W. Watts, and D. Kittelson. "Near Real-Time Ash Measurement. A Preliminary Study".November, Ecomondo , 2007.

Froelund, K., S. Fritz, and B. Smith. "Lubricating Oil Consumption Measurements on an EMD 16-645E Locomotive Diesel Engine." *ICE* 40 (2003): 361-8.

Froelund, K., et al. "Real-Time Transient and Steady-State Measurement of Oil Consumption for several Production SI Engines." *SAE International Spring Fuels and Lubricants Meeting and Exposition*.2001-01-1902 (2001)

Fuchs, N. A. "On the Stationary Charge Distribution on Aerosol Particles in a Bipolar Ionic Atmosphere " *Pure and Applied Geophysics* 56.1 (1963): 185.

Fulford, G., M. Moo-Young, and M. Bebu. "Thermophoretic Acceleration of Particle Deposition from Laminar Air Streams." *Canadian Journal of Chemical Engineering* 49 (1971): 553-6.

Gaiser, G., and P. Mucha. "Prediction of Pressure Drop in Diesel Particulate Filters Considering Ash Deposit and Partial Regenerations." *SAE Technical Paper Series* (2004)

Givens, W., et al. "Lube Formulation Effects on Transfer of Elements to Exhaust After-Treatment System Components." *Powertrain and Fluid Systems Conference and Exhibition* (2003)

Gligorijevic, R., J. Jevtic, and D. J. Borak. "Engine Oil Contribution to Diesel Exhaust Emissions." *Journal of Synthetic Lubrication* 23.1 (2006): 27-38.

Goldsmith, P., and F. May. "Aerosol Science." (1966)

Gordon, S., and B. McBride. *Computer Program for Calculation of Complex Chemical Equilibrium Compositions and Applications*. 1311 Vol. Cleveland, OH: NASA, 1994.

Gormley, P., and M. Kennedy. "Diffusion from a Stream Flowing through a Cylindrical Tube." *Proceedings of the Royal Irish Academy* 52A (1949): 163-9.

Heibel, A., and R. Bhargava. "Advanced Diesel Particulate Filter Design for Lifetime Pressure Drop Solution in Light Duty Applications." *Fuels and Emissions Conference* (2007)

Higgins, Kelly. "Kinetics of Diesel Nanoparticle Oxidation." *Environmental science technology* 37.9 (2003): 1949-54.

Hill, S., and S. Sytsma. "A Systems Approach to Oil Consumption." *SAE International Congress and Exposition* (1991)

Hinds, William C. *Aerosol Technology : Properties, Behavior, and Measurement of Airborne Particles*. 2nd ed. New York: Wiley, 1999.

Holman, J. P. *Heat Transfer*. 9th ed. New York: McGraw-Hill, 2002.

Ingham, D., and I. Pop. *Transport Phenomena in Porous Media*. Pergamon, 1998.

Ishizawa, T., et al. "Investigation into Ash Loading and its Relationship to DPF Regeneration Method." *SAE international journal of commercial vehicles* 2.2 (2010): 164-75.

Johnson, J. "Hydrocarbon Oxidation in a Diesel Catalytic Converter /." University of Minnesota, 1993. Minneapolis, MN: .

Johnson, T., et al. "A New Electrical Mobility Particle Sizer Spectrometer for Engine Exhaust Particle Measurements." *SAE Technical Paper Series* (2004)

Johnson, Timothy. "Diesel Emission Control in Review." *SAE international journal of fuels and lubricants* 2.1 (2009): 1-12.

Kim, J. "High Temperature Oxidation Method for Real-Time Measurement of Metallic Ash in Diesel Exhaust." Master of Science University of Minnesota, 2005.

Kimura, K., et al. "Real World Study of Diesel Particulate Filter Ash Accumulation in Heavy-Duty Diesel Trucks." *SAE Technical Paper Series* (2006)

Kingsley, R., T. Hands, and N. Collings. "A Fast Response Particulate Spectrometer for Combustion Aerosols." *SAE Technical Paper Series* (2002)

Kittelson, D., W. Watts, and J. Johnson. "On-Road and Laboratory Evaluation of Combustion Aerosols-Part1: Summary of Diesel Engine Results." *Journal of Aerosol Science* 37.8 (2006): 913-30.

Kittelson, David. "Engines and Nanoparticles: A Review." *Journal of Aerosol Science* 29.5 (1998): 575-88.

Knutson, E., and K. Whitby. "Aerosol Classification by Electric Mobility: Apparatus, Theory, and Applications." *Aerosol Science* 6 (1975): 443.

Koch, K. "Experience with Oil Consumption Measurements on the Engine Test Bed." *SAE Technical Paper Series* (1993)

Krause, W., et al. "Oil Separation in Crankcase Ventilation - New Concepts through System Analysis and Measurements." *SAE Technical Paper Series* (1995)

Lambert, C., et al. "Post Mortem of an Aged Tier 2 Light-Duty Diesel Truck Aftertreatment System." *SAE international journal of fuels and lubricants* 2.2 (2010): 167-75.

Lee, D., et al. "Characterization of Metal-Bearing Diesel Nanoparticles using Single-Particle Mass Spectrometry." *Journal of Aerosol Science* 37.1 (2006): 88-110.

Liu, G., M. Skemp, and J. Lincoln. "Diesel Particulate Filters: Trends and Implications of Particle Size Distribution Measurement." *SAE Technical Paper Series* (2003)

Lombaert, K., et al. "Nondestructive Analysis of Metallic Elements in Diesel Soot Collected on Filter: Benefits of Laser Induced Breakdown Spectroscopy." *Plasma Chemistry and Plasma Processing* 24.1 (2004): 41-56.

Manni, M., A. Pedicillio, and F. Bazzano. "A Study of Lubricating Oil Impact on Diesel Particulate Filters by Means of Accelerated Engine Tests." *SAE Technical Paper Series* (2006)

May, K. R. "COLLISON NEBULIZER: DESCRIPTION, PERFORMANCE AND APPLICATION." *Journal of Aerosol Science* 4.3 (1973): 235-43.

McBride, B., and S. Gordon. *Computer Program for Calculating and Fitting Thermodynamic Functions*. 1271 Vol. Cleveland, OH: NASA Glenn Research Center, 1992.

Miller, A., et al. "The Fate of Metal (Fe) during Diesel Combustion: Morphology, Chemistry, and Formation Pathways of Nanoparticles." *Combustion and Flame* 149.1 (2007): 129-43.

"Model 3010 Condensation Particle Counter; Instruction Manual." (2002)

"Model 3070A Elecitrical Aerosol Detector; a Fast Aerosol Concentration Detector for Wide Dynamic Range." (2004)

NEWMAN, J. *MASS TRANSFER TO THE REAR OF A CYLINDER AT HIGH SCHMIDT NUMBERS*. 8 Vol. , 1969.

Okada, S., et al. "Measurement of Trace Metal Composition in Diesel Engine Particulate and its Potential for Determining Oil Consumption: ICPMS and ATOFMS Measurements." *SAE Technical Paper Series* (2003)

Park, K., et al. "A Closure Study of Aerosol Mass Concentration Measurements: Comparison of Values obtained with Filters and by Direct Measurements of Mass Distributions." *Atmospheric Environment* 37.9 (2003): 1223-30.

Park, K., et al. "Relationship between Particle Mass and Mobility for Diesel Exhaust Particles." *Environmental science technology* 37.3 (2003): 577-83.

Pirro, D., A. Wessol, and J. Wills. *Lubrication Fundamentals*. 137 Vol. , 2001.

Sakurai, Hiromu. "On-Line Measurements of Diesel Nanoparticle Composition and Volatility." *Atmospheric Environment* 37.9 (2003): 1199-210.

Sappok, A., et al. "Characteristics and Effects of Ash Accumulation on Diesel Particulate Filter Performance: Rapidly Aged and Field Aged Results." *SAE Technical Paper Series* (2009)

Sappok, A., and V. Wong. "Detailed Chemical and Physical Characterization of Ash Species in Diesel Exhaust Entering Aftertreatment Systems." *SAE World Congress* (2007)

Series 3080 Electrostatic Classifiers Operation and Service Manual. Shoreview, MN: TSI Incorporated, 2008.

Shore, P. "Advances in the use of Tritium as a Radiotracer for Oil Consumption Measurement." *SAE Technical Paper Series* (1988)

Stetter, J., et al. "The Impact of Oil Consumption Mechanisms on Diesel Exhaust Particle Size Distributions and Detailed Exhaust Chemical Composition".August 2003, Newport, RI. Web.

Talbot, L. "THERMOPHORESIS OF PARTICLES IN A HEATED BOUNDARY LAYER." *Journal of Fluid Mechanics* 101.4 (1980): 737-58.

Varlot, K., et al. "Tibochemical Interactions between Micellar Calcium Borate and ZDDP: Evidence for Borophosphate Trobfilm by EELS". *Proceedings of the 25th Leeds-Lyon Symposium on Tribology.* Lyon, France. Elsevier Science B.V. , 1999. 433-438.

Wahiduzzaman, S., et al. "A Model for Evaporative Consumption of Lubricating Oil in Reciprocating Engines." *SAE Technical Paper Series* (1992)

Waldmann, L., and K. Schmitt. "Aerosol Science, Chapter 6." Ed. C. Davies., 1966.

Walker, K., G. Homsy, and F. Geyling. "Thermophoretic Deposition of Small Particles in Laminar Tube Flow." *Journal of colloid and interface science* 69.1 (1979): 138-47.

Wang, Y., et al. "Emissions of Fuel Metals Content from a Diesel Vehicle Engine." *Atmospheric Environment* 37.33 (2003): 4637-43.

Weng, W., and D. Richardson. "Cummins Smart Oil Consumption Measuring System." *SAE Technical Paper Series* (2000)

Wiedensohler, A. Weise, W., C. Helsper, and E. Luetkemeier. *DETERMINATION OF THE BIPOLAR CHARGE EQUILIBRIUM IN PURE GASES.*, 1986.

Wiedensohler, A. "APPROXIMATION OF THE BIPOLAR CHARGE DISTRIBUTION FOR PARTICLES IN THE SUBMICRON SIZE RANGE. ." *Journal of Aerosol Science* 19.3 (1988): 387-9.

Zehe, M., S. Gordon, and B. McBride. *CAP: A Computer Code for Generating Tabular Thermodynamic Functions from NASA Lewis Coefficients*. 2001-210959 Vol. Cleveland, OH: NASA Glenn Research Center, 2001.

Appendix A

Thermophoretic penetration derivation

The thermophoretic force acting on a spherical particle is given by Equation 14, where d_p is the particle diameter, p is the gas pressure, T is the absolute particle temperature, ∇ T is the thermal gradient, and λ is the gas mean free path. The thermophoretic velocity from Waldmann and Schmitt (1966) is shown in Equation 15, where η is the viscosity of the gas. These equations are for particles in the Stoke's regime where the particle diameter is less than the mean free path the gas molecules.

$$F_{th} = \frac{p\lambda d_p^{\,2}\nabla T}{T} \text{ for } d_p < \lambda \tag{14}$$

$$V_{th} = \frac{-0.55\eta\nabla T}{\rho_g T} \text{ for } d_p < \lambda \tag{15}$$

Johnson (1993) laid out a method for calculating the thermophoretic particle loss in a channel. Equation 16 can first be written for the conservation of particle number through a section of tube with the diameter d. The equation is then simplified into an easier integral form shown in Equation 17. The particle number concentration is represented by n. Q is the volumetric flowrate and s is the axial distance.

$$Qn = Q(n + \Delta N) + V_t n \pi d \Delta s \tag{16}$$

$$\frac{dn}{n} = \frac{-V_t \pi d}{Q} ds \tag{17}$$

The conservation of energy between the hot aerosol and the cooler tube wall can also be carried out. Newton's law of cooling is expressed in Equation 18 (Holman, 2002) where A is the surface area, h is the heat transfer coefficient, and the T's are the respective temperatures. Equation 19 shows the substitution for q and A in Equation 18 for the specific case of the heated aerosol traveling through a cooler tube. Under the assumption that the volume fraction of particles in the aerosol is very small, the properties for density ρ and specific heat cp should be taken for the gas.

$$q = hA(T_w - T_\infty) \tag{18}$$

$$\rho Q c_p dT = -h\pi d(T_w - T_\infty)ds \tag{19}$$

Equation 20 displays the result of combining the previous equations. Equation 21 can be formed by substituting in for Vt.

$$\frac{dn}{n} = \frac{-V_t \rho c_p}{h} \frac{dT}{(T - T_w)} \tag{20}$$

$$\frac{dn}{n} = \frac{-K_t v \rho c_p}{h} \frac{\nabla T}{T} \frac{dT}{(T - T_w)} \tag{21}$$

The thermal gradient can be substituted for using the following process. First, the energy balance can be written as shown in Equation 22.

$$-k \frac{dT}{dr}_{wall} = h(T - T_w) \tag{22}$$

The thermal gradient can be substituted for as shown in Equation 23.

$$\nabla T = \frac{dT}{dr}_{wall} \tag{23}$$

Equation 24 shows the proceeding substitution of for the thermal gradient into Equation 21.

$$\frac{dn}{n} = \frac{-K_t v \rho c_p}{k} \frac{1}{T} dT \tag{24}$$

Equation 25 shows the integrated form of Equation 24. This is then simplified in the steps shown in Equations 26 and 27, where Pr is the Prandtl number, the ratio of the momentum diffusivity to the thermal diffusivity.

$$\ln\left(\frac{n_o}{n_i}\right) = \frac{-K_t v \rho c_p}{k} \ln\left(\frac{T_o}{T_i}\right) \tag{25}$$

$$\left(\frac{n_o}{n_i}\right) = \left(\frac{T_o}{Ti}\right)^{\frac{-K_t v \rho c_p}{k}} \tag{26}$$

$$\left(\frac{n_o}{n_i}\right) = \left(\frac{T_o}{Ti}\right)^{\Pr K_t} \tag{27}$$

Equation 27 can be used to calculate and correct for the thermophoretic particle loss downstream of a heated portion of an aerosol sampling system when the hot aerosol is cooled to a lower temperature.

Appendix B

Overview and theory of relevant particle instruments

Another important force that acts on particles is electrostatic. Some particles have more or less electrons than necessary to have a neutral charge. When encompassed in an electric field or near another charged particle, a net force acts on charged particles. These forces can be taken advantage of for classifying particles of specific sizes or electrical equivalent sizes and for making particle size distribution measurements.

The electrostatic force acting on a particle is shown by Equation 28 where e is the smallest unit of charge (1.6 x 10^{-19} C), n is the number of charges on the particle, and E is the strength of the electric field.

$$F_E = neE \tag{28}$$

For a particle in the Stoke's regime the electrostatic force and drag forces can be balanced as shown in Equation 29. The velocity can then be solved for as shown in Equation 30. Equation 31 substitutes the particle mobility B into Equation 30.

$$neE = \frac{3\pi\eta V d}{C_c} \tag{29}$$

$$V_{TE} = \frac{neEC_c}{3\pi\eta d} \tag{30}$$

$$V_{TE} = neEB \tag{31}$$

The electrical mobility of a particle is shown in Equation 32.

$$Z = neB \tag{32}$$

For concentric cylinders where the center rod is charged and the outer rod is neutral, Equation 33 shows the strength of the electric field. V is the voltage potential between the cylinders, r is the radial distance from the center axis and R_1 and R_2 are the inner and outer cylinder radii respectively.

$$E = \frac{V}{r \ln\left(\frac{R_2}{R_1}\right)} \tag{33}$$

The radial velocity in terms of the radial position is given in Equation 34. The trajectory for a particle moving through the concentric cylinders is shown by Equation

35. These principals are applied to particle measurement instrumentation such as the differential mobility analyzer (DMA) and scanning mobility particle sizer (SMPS).

$$v(r) = \frac{ZV}{r \ln\left(\frac{R_2}{R_1}\right)} \tag{34}$$

$$\frac{dr}{dx} = \frac{ZV}{ru(r) \ln\left(\frac{R_2}{R_1}\right)} \tag{35}$$

The DMA is used to classify particles by mobility diameter. Figure 41 shows the diagram and flow schematic of a TSI 3080 Electrostatic Classifier with a long column DMA. The DMA consists of a charged center rod with a neutral outer cylinder. The sample aerosol is first passed through an impactor that removes larger particles with a specific size cut. Next, the aerosol passes through a neutralizer that gives the particles a known equilibrium charge distribution based on Wiedensohler et al. (1986), Weidensohler (1988), and Fuchs (1963). The two flows enter the top of the classifier column. The majority of the flow is a laminar filtered sheath air. The aerosol is introduced on the outer edge of the top of the column. As the particles flow through the column, positively charged particles will have a velocity vector in the direction of the negatively charged center rod. Depending on the flows and the charge of the center rod, particles of a narrow band of mobility will enter a small slit at the bottom of the column. The remaining particles will either exit through the excess flow or migrate to the center rod before the bottom of the column. Knowing the flow rates through the column and the column geometry, the mobility diameter of the classified particles can be calculated. The derivation of the particle paths in a DMA and the transfer function of the probability that a particle entering the column of a specific mobility will exit through the slit with the outlet sample flow is explained in detail in Knutson and Whitby (1975).

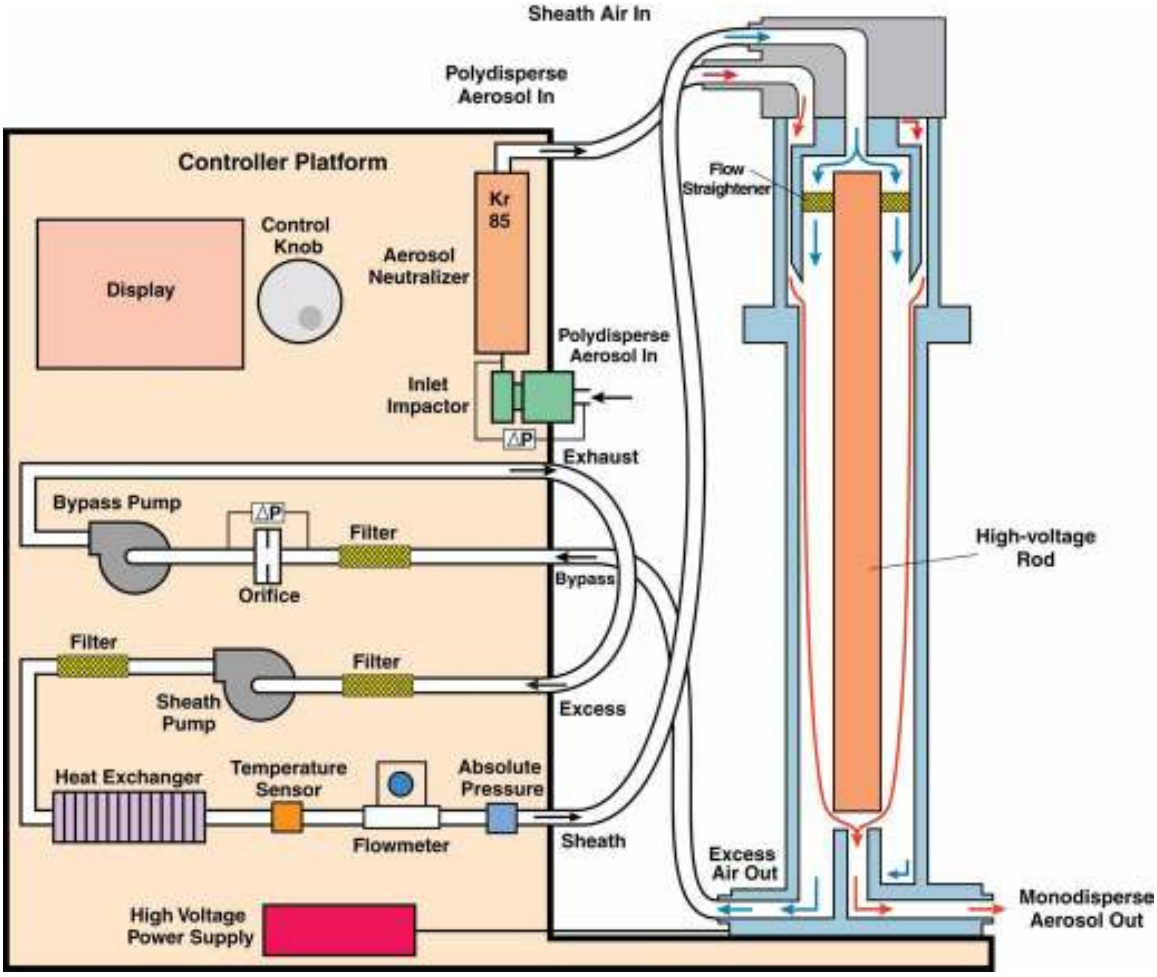

Figure 41: Diagram of differential mobility analyzer (DMA) (TSI Incorporated, 2008)

In a SMPS the particles in the sample flow exiting the DMA are counted with a CPC. A schematic for a specific continuous flow CPC is shown in Figure 42. For most continuous flow CPCs, the sample air is passed through a heated saturator where a fluid such as water or n-butanol is heated. The sample is subsequently cooled creating a supersaturated vapor. The vapor condenses on the particles, growing them to an optically detectable size. An overview of nucleation and particle growth by condensation can be found in Hinds (1999). If grown to 12 μm, particles are detectable with a light-scattering system (Baron and Willeke, 2001). The light-scattering system can function as an individual particle counter for concentrations below 10^3 particles/cm^3. For higher concentrations the photo-detector functions as a photometer (Baron and Willeke, 2001).

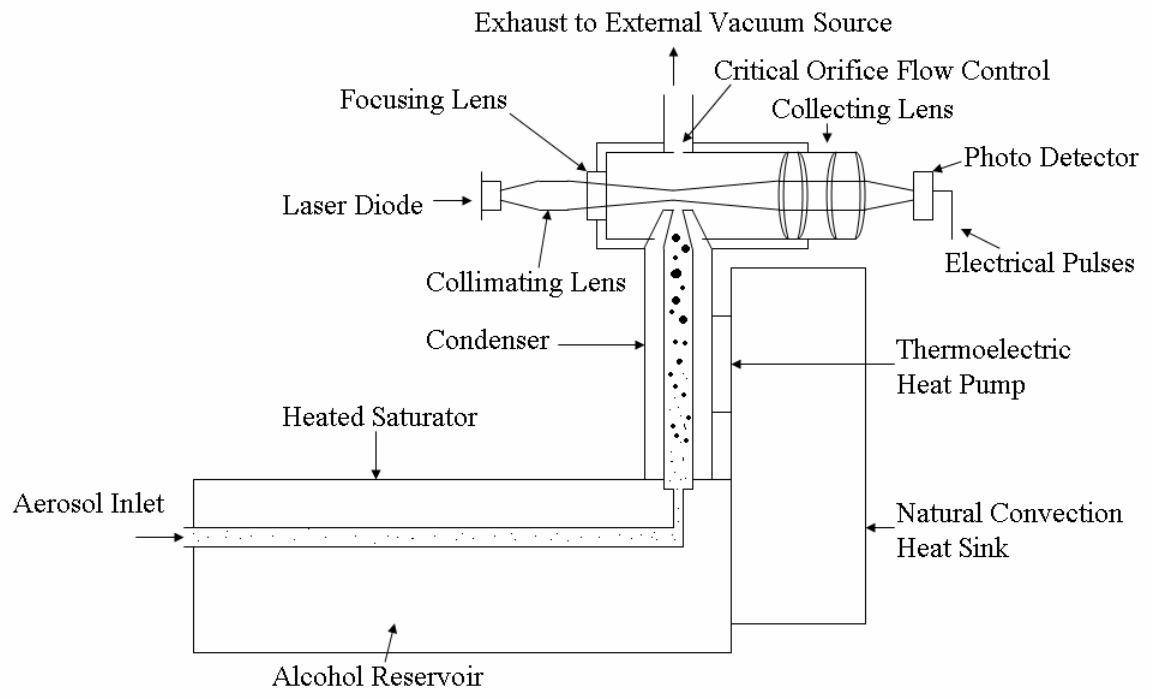

Figure 42: Flow schematic of a TSI model 3010 CPC (TSI Incorporated, 2002)

The SMPS can allow for the construction of a particle size distribution by exponentially varying the voltage of the DMA rod while using a CPC to continuously monitor the particle concentrations of the classified particles exiting the DMA column. Mean particle diameters are used for individual particle size channels, with the resolution ranging from 8 to 64 channels/decade. By integrating these distributions total particle number concentrations can be found. Surface area and volume distributions can be constructed from the number distributions by converting each size bin to its corresponding surface area or volume using a geometric factor. If the particle densities are known mass distributions and concentrations can be calculated as well.

Because of the scanning nature of the SMPS, the size distribution information is composed of sections of the distribution sampled at different times. This is acceptable for a steady aerosol, but for transient aerosols a faster time response is desired. Other instruments were used to make real-time particle measurements. A stand alone CPC and EAD were also used at times. The EAD charges particles using a corona needle, captures

the particles on an electrometer, and measures the total current, relating it to particle diameter (d^1) concentrations.

Appendix C

Table 12: Common ICP-MS detectibility limits

Element	Detectibility limit
Ca	0.1 - 1 ppt
Mg	< 0.1 ppt
P	10 - 100 ppt
S	0.1 - 1 ppb
Zn	0.1 - 1 ppt
B	1 - 10 ppt
Fe	0.1 - 1 ppt
Si	10 - 100 ppt
Na	0.1 - 1 ppt